A&A 660, A81 (2022)
https://doi.org/10.1051/0004-6361/202142048

Astronomy & Astrophysics

Radio footprints of a minor merger in the Shapley Supercluster: From supercluster down to galactic scales

T. Venturi[1], S. Giacintucci[2], P. Merluzzi[3], S. Bardelli[4], G. Busarello[3], D. Dallacasa[5,1], S. P. Sikhosana[6,7], J. Marvil[8], O. Smirnov[9,10], H. Bourdin[11], P. Mazzotta[11], M. Rossetti[12], L. Rudnick[13], G. Bernardi[1,9,10], M. Brüggen[14], E. Carretti[1], R. Cassano[1], G. Di Gennaro[15,14], F. Gastaldello[12], R. Kale[16], K. Knowles[9,10], B. S. Koribalski[17,18], I. Heywood[19,20,10], A. M. Hopkins[21], R. P. Norris[18,17], T. H. Reiprich[22], C. Tasse[23,24], T. Vernstrom[25], E. Zucca[4], L. H. Bester[10,9], J. M. Diego[26], and J. Kanapathippillai[25]

(Affiliations can be found after the references)

Received 20 October 2021 / Accepted 9 December 2021

ABSTRACT

Context. The Shapley Supercluster ($\langle z \rangle \approx 0.048$) contains several tens of gravitationally bound clusters and groups, making it an ideal subject for radio studies of cluster mergers.

Aims. We used new high sensitivity radio observations to investigate the less energetic events of mass assembly in the Shapley Supercluster from supercluster down to galactic scales.

Methods. We created total intensity images of the full region between A3558 and A3562, from ∼230 to ∼1650 MHz, using ASKAP, MeerKAT and the GMRT, with sensitivities ranging from ∼6 to ∼100 μJy beam^{-1}. We performed a detailed morphological and spectral study of the extended emission features, complemented with ESO-VST optical imaging and X-ray data from *XMM-Newton*.

Results. We report the first GHz frequency detection of extremely low brightness intercluster diffuse emission on a ∼1 Mpc scale connecting a cluster and a group, namely: A3562 and the group SC 1329–313. It is morphologically similar to the X-ray emission in the region. We also found (1) a radio tail generated by ram pressure stripping in the galaxy SOS 61086 in SC 1329–313; (2) a head-tail radio galaxy, whose tail is broken and culminates in a misaligned bar; (3) ultrasteep diffuse emission at the centre of A3558. Finally (4), we confirm the ultra-steep spectrum nature of the radio halo in A3562.

Conclusions. Our study strongly supports the scenario of a flyby of SC 1329–313 north of A3562 into the supercluster core. This event perturbed the centre of A3562, leaving traces of this interaction in the form of turbulence between A3562 and SC 1329–313, at the origin of the radio bridge and eventually affecting the evolution of individual supercluster galaxies by triggering ram pressure stripping. Our work shows that minor mergers can be spectacular and have the potential to generate diffuse radio emission that carries important information on the formation of large-scale structures in the Universe.

Key words. galaxies: clusters: general – galaxies: clusters: individual: A3558 – galaxies: clusters: individual: A3562 – galaxies: clusters: individual: SC 1329–313 – galaxies: clusters: individual: SC 1327–312 – radio continuum: galaxies

1. Introduction

According to the hierarchical scenario for the formation of large-scale structures, galaxy clusters form as a consequence of mergers to reach and exceed masses of the order of $10^{15}\,M_{\odot}$. With a total energy output of the order of 10^{63}–10^{64} erg, cluster mergers are the most energetic events in the Universe. The gravitational energy released into the cluster volume during such events deeply affects the dynamics of the galaxies, as well as the properties of the thermal and non-thermal (relativistic particles and magnetic field) components of the intracluster medium (ICM).

The close connection between the properties of the radio emission in galaxy clusters and their dynamical state is now an established result. In particular, giant radio halos and relics – Mpc-scale synchrotron steep-spectrum (α typically in the range $[-1.4, -1.2]$ for $S \propto \nu^{\alpha}$) radio sources of μJy arcsec^{-2} surface brightness and below (see van Weeren et al. 2019 for a recent observational overview) – are thought to be the result of particle re-acceleration due to turbulence and shocks induced in the cluster volume during mergers and accretion processes (see Brunetti & Jones 2014 for the most recent theoretical review). While the details of the microphysics of these processes are still being investigated, the connection between radio halos, relics, and cluster mergers is supported by a number of observational results and statistical investigations as per Schuecker et al. (2001), Cassano et al. (2010), Kale et al. (2015), as well as studies on several individual clusters (e.g. A521, Bourdin et al. 2013; A1682, Clarke et al. 2019; A2256, Ge et al. 2020). The former results show that the number of radio halos is a steep function of the cluster mass and their detection in merging clusters increases considerably for masses $M \gtrsim 8 \times 10^{14}\,M_{\odot}$ (see Liang et al. 2000; Buote 2001 and more recently Cuciti et al. 2021; Duchesne et al. 2021a; van Weeren et al. 2021). Moreover, it has been shown that less massive and/or less energetic mergers may lead to the formation of radio halos with ultra-steep spectra, as found in A521, whose spectrum with $\alpha \sim -1.9$ makes it a prototype for ultra-steep spectrum radio halos (Brunetti et al. 2008; Dallacasa et al. 2009).

Most of our current knowledge on the connection between cluster mergers and diffuse cluster radio sources is built upon observations of samples of intermediate to massive clusters, namely, $M \gtrsim 6$–$8 \times 10^{14}\,M_{\odot}$, and characterised by mergers with

a moderate mass ratio ($M_2/M_1 \geq$ 1:4−1:5; i.e. Cassano et al. 2016). However, the dominant (i.e. most frequent) process of mass assembly in the Universe is the accretion of systems in less extreme processes involving either smaller masses or mass ratios well below 1:4−1:5, namely, so-called 'minor mergers'. The steep relation between the cluster mass (or X-ray luminosity) and the radio power for radio halos (i.e. Cuciti et al. 2021) and relics (i.e. de Gasperin et al. 2014; Duchesne et al. 2021b), along with the limited sensitivity of radio interferometers has made the detection of such sources in less massive systems an extremely challenging task thus far and the observational signatures of minor mergers are still largely unexplored.

Against this backdrop, we can also see that a new era has just begun. The substantial leap forward in sensitivity and u−v coverage offered by current interferometers – such as LOw Frequency ARray (LOFAR, van Haarlem et al. 2013), Australian Square Kilometre Array Pathfinder (ASKAP, Hotan et al. 2021), MeerKAT (Camilo et al. 2018), and the upgraded Giant Metrewave Radio Telescope (uGMRT) – is considerably broadening the observational parameter space and opening a new window on phenomena that have been inaccessible thus far. Radio bridges of extremely low surface brightness are being discovered (i.e. A1758, Botteon et al. 2020a; A399–A401, Govoni et al. 2019) and, in addition, extremely long and twisted tailed radio galaxies as well as ultra-steep spectrum radio filaments are shown to be common inhabitants of galaxy clusters (i.e. A2034, Shimwell et al. 2016; Perseus, Gendron-Marsolais et al. 2020; A2255, Botteon et al. 2020b).

To take advantage of these new capabilities, we observed the central region of the Shapley Supercluster with ASKAP, MeerKAT, and GMRT in search of radio signatures of merger events in low- to intermediate-mass environments. In this paper, we focus on the A3558 cluster complex in the central region of the Shapley Supercluster and we report on the findings in the whole region, which includes the two clusters A3558 and A3562, and the two groups SC 1327–312 and SC 1329–313 between them. The layout of the paper is as follows. In Sect. 2, we provide an overview of the region of the Shapley Supercluster that is under investigation. In Sect. 3, we describe the radio observations and the data analysis. The radio images and spectral analysis are presented in Sect. 4. Our findings are discussed in Sect. 5. Conclusions are given in Sect. 6.

Throughout the paper, we use the spectral power-law convention $S_\nu \propto \nu^\alpha$ and assume a cosmology based on $H_0 = 70\,\mathrm{km\,s^{-1}\,Mpc^{-1}}$, $\Omega_\mathrm{m} = 0.3$, and $\Omega_\Lambda = 0.7$. At the average redshift of the Shapley Supercluster, that is, $z = 0.048$, this gives a conversion factor of 0.928 kpc arcsec^{-1} and a luminosity distance of 210 Mpc.

2. Shapley Supercluster in context

The Shapley Supercluster (Shapley 1930) is one of the richest and most massive concentrations of gravitationally bound galaxy clusters in the local Universe (i.e. Scaramella et al. 1989; Raychaudhury 1989; Vettolani et al. 1990; Zucca et al. 1993). It is located in the southern sky and lies behind the Hydra-Centaurus cluster. Overall, the structure covers a redshift range $0.033 \lesssim z \lesssim 0.06$ (Quintana et al. 1995, 1997), and has a mean redshift of $z \approx 0.048$.

Due to the very high overdensity and large number of galaxy clusters, and also thanks to its proximity, it is an ideal place to start investigating the effects of group accretion and cluster minor mergers, as is clear from the masses and bolometric X-ray luminosities of the individual clusters and groups, which

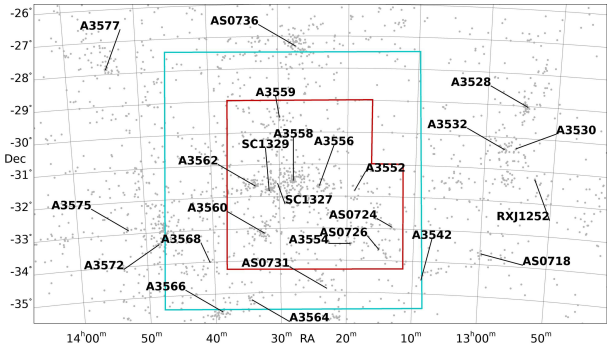

Fig. 1. Location of the clusters and groups in the Shapley Supercluster. The redshift information is from the 6dF Galaxy Survey (6dFGS, Jones et al. 2009). The redshift range considered is 0.035−0.060. The cyan lines highlight the area covered by the ASKAP observations (Sect. 3.1), the red lines highlight the coverage of the ESO-VST optical imaging of ShaSS (Merluzzi et al. 2015).

range (estimated using 11 clusters, including A3552, see Fig. 1) between $M_{500} \approx 0.4$−$9.8 \times 10^{14}\,M_\odot$ (Higuchi et al. 2020)[1], and $L_X \approx 0.4$−6.7×10^{44} erg s^{-1} (De Filippis et al. 2005) respectively, across 260 Mpc^2 around the supercluster core.

The A3558 cluster complex is the centre of the Shapley Supercluster. It consists of a chain of three ACO (Abell et al. 1989) clusters (A3556, A3558 and A3562) and two smaller groups (SC 1327–312 and SC 1329–313). It is extended for a projected length of about 7.5 h^{-1} Mpc in the east-west direction at an average redshift of $\langle z \rangle \approx 0.048$. Figure 1 shows the clusters and groups in the Shapley Supercluster. The cyan lines highlight the area covered by the ASKAP observations (Sect. 3.1) and the red lines highlight the area of the Shapley Supercluster Survey (ShaSS, Merluzzi et al. 2015; Mercurio et al. 2015), which includes optical imaging from ESO-VLT Survey Telescope (VST). The main properties of the clusters studied in this paper are reported in Table 1.

Several studies in the infrared and visibile (Bardelli et al. 1998a,b; Merluzzi et al. 2015; Haines et al. 2018; Higuchi et al. 2020), X-ray (Markevitch & Vikhlinin 1997; Ettori et al. 2000; Finoguenov et al. 2004; Rossetti et al. 2007; Ghizzardi et al. 2010), and radio (Venturi et al. 2000, 2003, hereinafter V03; Giacintucci et al. 2004, 2005, hereinafter G05; Venturi et al. 2017a, hereinafter V17) have provided observational evidence in support of the idea that merging and accretion processes are taking place in the whole region between A3558 and A3562. This portion of the Shapley Supercluster has also been detected by *Planck* (see Fig. 1 in Planck Collaboration XXIX 2013). On the western end of the chain, the cluster A3556 is rather faint in X-rays and shows a dynamically relaxed state. The radio properties of the dominant galaxy in A3556 are consistent with its relaxed dynamical state as derived from the X-ray (Venturi et al. 1996; Di Gennaro et al. 2018).

3. Observations and data analysis

The findings presented in this paper are based on five different datasets, collected with GMRT, ASKAP, and MeerKAT, and cover a frequency range between 230 MHz to 1.65 GHz. The details of our observations and final images are reported in

[1] The dynamical masses presented in Higuchi et al. (2020) have been transformed to M_{500} by means of the software hydro_mc (github.com/aragagnin/hydro_mc) by Ragagnin et al. (2021).

Table 1. Properties of the clusters.

Cluster name	RA_{J2000} (^{h,m,s})	Dec_{J2000} ($^\circ,',''$)	v (km s^{-1})	σ_v (km s^{-1})	$L_{X,bol}$ (10^{44} erg s^{-1})	M_{500} (10^{13} $M_\odot$)
A3558	13 28 02	−31 29 35	14 500 ± 40	1007 ± 30	6.68	98 ± 9
SC 1327–312	13 29 45	−31 36 13	14 800 ± 40	535 ± 20	1.27	20 ± 2
SC 1329–313	13 31 36	−31 48 45	13 400 ± 50	373 ± 30	0.52	5 ± 1
A3562	13 33 47	−31 40 37	14 800 ± 55	769 ± 30	3.31	44 ± 5

Notes. Cluster coordinates are taken from Merluzzi et al. (2015). Values for v and σ_v are taken from Haines et al. (2018), $L_{X,bol}$ from De Filippis et al. (2005). M_{500} is derived from M_{dyn} in Higuchi et al. (2020) by means of the package hydro_mc (Ragagnin et al. 2021).

Table 2. Logs of the observations and image parameters.

Cluster	Pointing centre RA, Dec (J2000)	Array	Project	Obs. date	ν [a] (MHz)	$\Delta\nu$ [b] (MHz)	t_{int} (h)	*FWHM* (″, °)	rms (μJy beam^{-1})
A3558	13 25 51, −31 03 05	ASKAP	ESP 20	19-Mar.-19	887	288	11	13.2 × 10.4, 85.4	∼30–50
A3558	13 27 54, −31 29 32	GMRT	22_039	30-Aug.-12	306	32	7	14.0 × 9.5, 18.4	∼60–100
		GMRT	22_039	02-May-15	608	32	5	10.9 × 5.6, 35.2	∼100
	13 27 54, −31 29 32	MeerKAT	[c]	04-Jul.-18	1283	856	2	7.0 × 5.9, 1.9	∼6
SC 1329–313	13 31 30, −31 44 00	GMRT	30_024	21-May-16	607	33	7	6.3 × 3.2, 0	∼50
		GMRT	30_024	22-May-16	233	33	7	24.4 × 10.7, 26	∼500
	13 31 08, −31 40 23	MeerKAT	[d]	06-Jul.-18	1283	856	8	7.3 × 7.2, 84.1	∼6
A3562	13 33 35, −31 40 30	MeerKAT	AO 1 [e]	07-Jul.-19	1283	856	10	6.9 × 6.5, 151.8	∼6

Notes. [a] and [b]refer to the central frequency and total bandwidth respectively. [c]The pointing is part of the MeerKAT scientific commissioning. [d]The pointing is part of the MeerKAT Galaxy Clusters Legacy Survey. [e]Observations obtained by the authors in response to the January 2019 MeerKAT Announcement of Opportunity.

Table 2. A description of the observational setup, calibration, imaging and mosaicing for each dataset is provided in the following subsections, together with details on the data analysis of the *XMM-Newton* observations used in the discussion.

3.1. ASKAP

The core of the Shapley Supercluster was observed with ASKAP as part of the EMU Early Science programme (Norris et al. 2011; Jonhnston et al. 2008) ESP 20. The observations (Table 2) were carried out on 19 March 2019 (scheduling block 8140) with 35 out of the 36 antennas in the array. The antenna configuration provides a baseline coverage that ranges from ∼22 m to ∼6.4 km. For this set of observations, the ASKAP correlator was used in pseudo-continuum mode to provide 288 channels, each with 1 MHz bandwidth, centred on 887 MHz. The telescope was configured to produce 36 electronically formed beams arranged on the sky in a 6 × 6 square grid; each individual beam covers an area of ∼1 deg^2, giving a total instantaneous field of view of ∼31 deg^2 (Hotan et al. 2021).

At the beginning of each observation, the source B1934–638 was observed for 3 min at the centre of each beam to calibrate the delay, phase, bandpass, and flux-density, based on the model from Reynolds (Reynolds 1994). The data reduction was performed using the ASKAPsoft software package and associated processing pipelines[2]. Images were produced using the w-projection algorithm to account for the w-term in the Fourier transform and with robust imaging weights to suppress the sidelobes of the point spread function. The deconvolution process used the clean algorithm and included two Taylor terms to model the spectral variation of sources and several Gaussian scales to model the structure of extended sources. Calibration and imaging were carried out separately for each beam, including one round of phase-only self-calibration, after which the images were combined with a linear mosaic to produce the final image. A comparison between mosaics generated using simple 2d Gaussian beam models versus newer holograghy beam models using a large number of bright sources allows us to state that the residual amplitude calibration errors are of the order of 5%.

The centre of our final mosaic, which is shown in Fig. 2, is $RA_{J2000} = 13^h25^m50^s$, $Dec_{J2000} = -31^\circ03'05''$. The black contours in the image show the galaxy number density of the supercluster members (Haines et al. 2018). The field of view of the ASKAP image covers most of the supercluster, as is clear from Fig. 1. The angular resolution is 13.2″×10.4″ and the noise level is in the range 30–50 μJy beam^{-1}. As seen in Fig. 2, the overall quality of the image is affected by the presence of the strong and extended radio galaxy PKS 1333–33 (Killeen & Bicknell 1988; Condon et al. 2021) located at the south–eastern edge of the field of view. Moreover, artefacts in the shape of ripples in the north–south direction are also present.

The goals of our ASKAP Early Science Project are multifold. In this paper, we focus on the diffuse and extended emission associated with both the ICM and individual galaxies in the region between A3562 and SC 1329–313 (zoomed in the upper panel of Fig. 3) and in A3558 (upper panel of Fig. 4). A detailed analysis of the radio galaxy population and the role of the environment by means of the ShaSS dataset is in preparation.

3.2. MeerKAT

The MeerKAT observations come from various projects, as clarified in the notes to Table 2. Our observations on

[2] https://www.atnf.csiro.au/computing/software/askapsoft/sdp/docs/current/

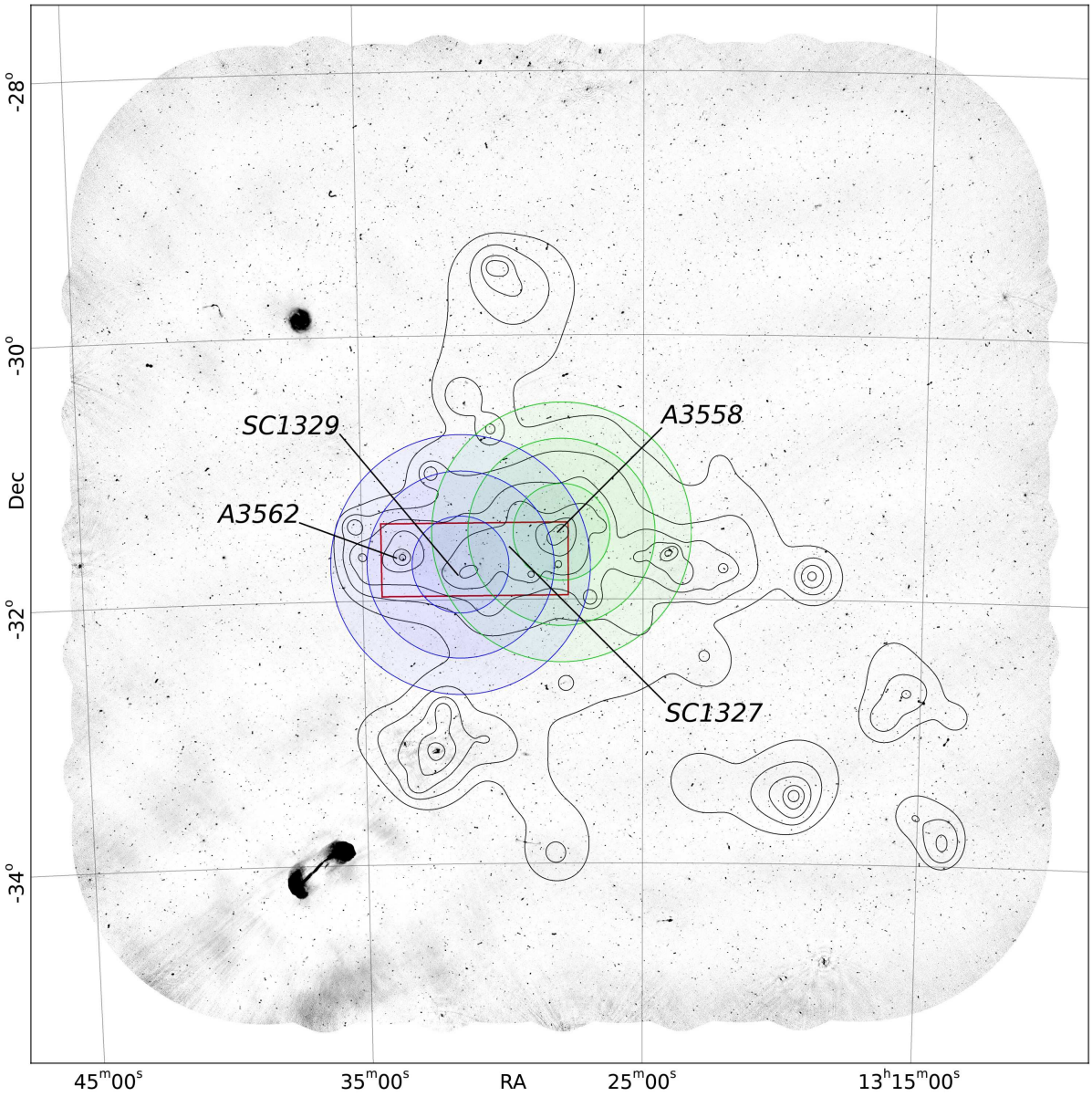

Fig. 2. Grey-scale view of the full field imaged by ASKAP at 887 MHz. The restoring beam is 13.2″ × 10.4″, p.a. 85.4°. The noise level ranges between 30 and 50 μJy beam^{-1} across the field. The radio galaxy PKS 1333–33 is clearly visible in the bottom–left part of the field. The black contours show the number density of the galaxies at the redshift of the Shapley Supercluster. The contours correspond to 5, 10, 20, 40, 80, 160 gal Mpc^{-2} (Haines et al. 2018). The region under study in this paper, going from A3562 to the central part of A3558 (east to west) is highlighted in the red rectangle. The green and purple circles show the GMRT pointings of the observations 22_039 and 30_024 respectively, and the full area covered by the primary beam.

A3562, carried out in July 2019 (see Table 2), were complemented with observations centered on SC 1329–313 and A3558 as part of the MeerKAT Galaxy Cluster Legacy Survey (MGCLS, Knowles et al. 2022) and of the MeerKAT scientific commissioning.

The July 2019 observations were reduced as follows. We used the CARACAL pipeline[3] (Józsa et al. 2020, 2022) for the initial data reduction. CARACAL orchestrates standard reduction packages into a single workflow. In this instance, it combined the TRICOLOUR[4] flagger (Hugo et al. 2022) for RFI flagging, and standard CASA tasks for reference calibration. The Perley & Butler (2013) scale was used to set the flux density scale of B1934–638. Whereas for the other standard MeerKAT flux density calibration source, PKS 0408–65, we used a custom component-based field model provided in CARACAL, converted into model visibilities via the MEQTREES package (Noordam & Smirnov 2010). After applying all the reference calibrations, the data were averaged from the initial 4096 to 1024 channels, and imaged using the WSCLEAN package (Offringa et al. 2014). We used Briggs weighting, robust = 0. We employed the joined-channel deconvolution and (4th order) polynomial fitting options of WSCLEAN and made wideband images. We imaged an area of ≈2.°2 × 2.°2. This was followed by a round of phase and delay self-calibration using the CUBICAL[5] package (Kenyon et al. 2018).

[3] https://github.com/caracal-pipeline/caracal
[4] https://github.com/ska-sa/tricolour
[5] https://github.com/ratt-ru/cubical

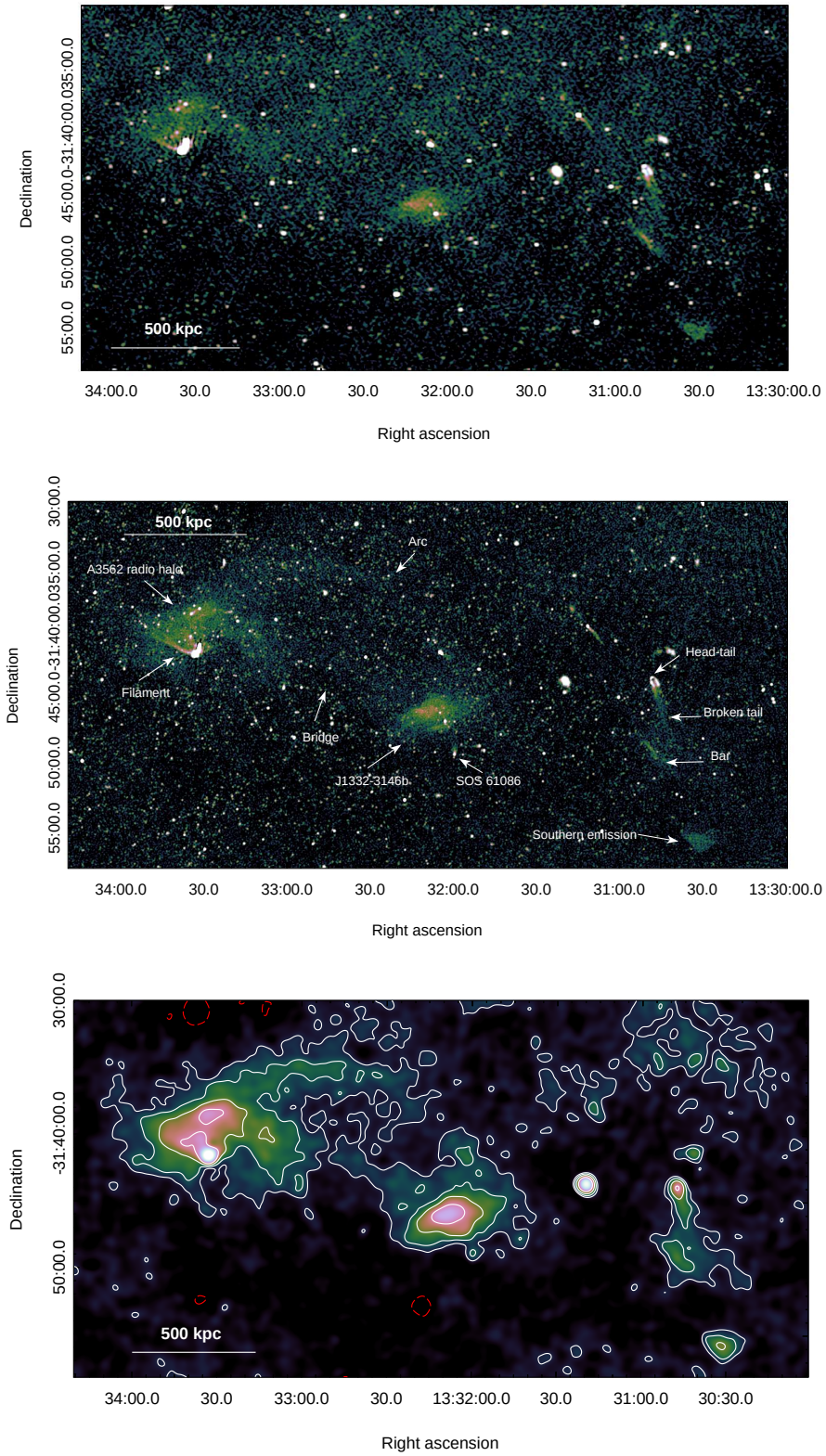

Fig. 3. Colour scale of the 887 MHz ASKAP image zoomed into the area encompassing A3562 and SC 1329–313 (*upper panel*). Restoring beam and noise level are as in Fig. 2. *Central panel*: the 1.28 GHz MeerKAT image of the same region. The restoring beam is $6.9'' \times 6.5''$, p.a. 151.8°. The average noise level is $\sim$6 μJy beam^{-1}. The flux density colour scale is in the range −0.1 to 0.7 mJy. The labels highlight the features presented in this paper. *Bottom panel*: the colour scale of the 1.28 GHz MeerKAT filtered image of the same region, convolved with a beam of $40'' \times 40''$ (see Sect. 3.2), with contours (dashed red for negative) of the same image overlaid. The contours are plotted at ±0.1, 0.2, 0.4, 0.8 mJy beam^{-1}, the average noise level is $\sim$30 μJy beam^{-1}.

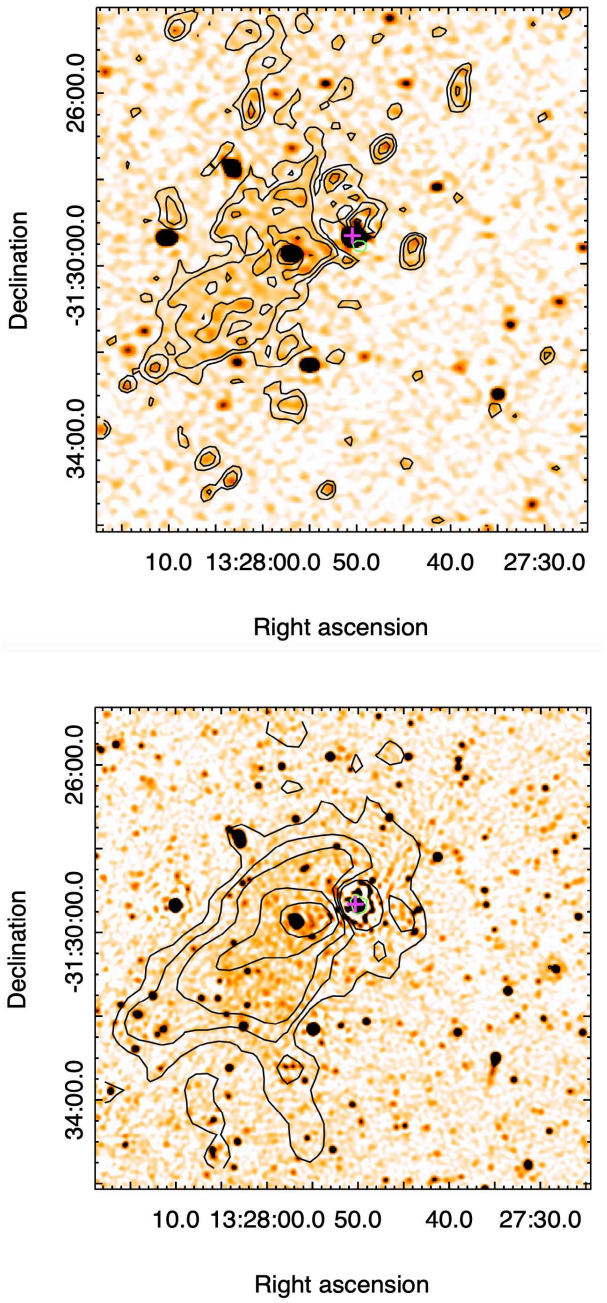

Fig. 4. Radio halo in A3558. In both panels the magenta cross shows the position of the brightest cluster galaxy (BCG). *Upper panel*: ASKAP image at 887 MHz in colour (same resolution and rms as in the upper panel of Fig. 3). The black contours show the emission of the halo after subtraction of the embedded point sources (see Sect. 4.7). The resolutions is 25.1″ × 20.9″, in p.a. 131.5° and the rms is ∼35 μJy beam^{-1}. Contour levels start at ±0.15 mJy beam^{-1} and are spaced by $\sqrt{2}$ (negative contours in green). *Lower panel*: MeerKAT image at 1.283 GHz in colour (same resolution and rms as in the central panel of Fig. 3). The black contours show the emission after subtraction of the point sources (see Sect. 4.7) convolved with a restoring beam of 40.9″×40.4″, in p.a. 144.6°. The rms is ∼35 μJy beam^{-1}. Contour levels start at ±0.125 mJy beam^{-1} and are spaced by $\sqrt{2}$ (negative contours in green).

The data reduction of the pointings belonging to the MGCLS has been described in detail in Knowles et al. (2022). The available products include in-band spectral index information $\alpha^{1656\,\mathrm{MHz}}_{908\,\mathrm{MHz}}$ within 36′ from the pointing centres, and band-averaged Stokes *I*, *Q*, *U*, and *V* images.

To double-check the consistency with the data analysis, the original *u*−*v* data of the MGCLS pointings were passed through the pipeline developed by SARAO, with comparable results. Both approaches produce images of extremely high quality, with rms values very close to the thermal noise, i.e. rms ∼6 μJy beam^{-1} at full resolution (see Table 2). To enhance the low-surface brightness emission in the field, we produced MGCLS images convolved to a resolution of 15″. The average noise at this lower resolution is in the range ∼15−30 μJy beam^{-1}. The average residual amplitude calibration errors are of the order of 5% for all MeerKAT datasets.

We finally produced images at the resolution of 40″ × 40″ after removing the contribution of the individual sources. We followed two different approaches. We adopted both (1) the filtering method described in Rudnick (2002) and (2) the subtraction of individual galaxies from the *u*−*v* plane with further convolution of the residual emission (see Venturi et al. 2007). The resulting images are consistent in the morphological details, but differ slightly in the flux densities integrated over large areas, the first method providing slightly higher values. Considering the very different approach of the two methods, we assume a conservative flux density uncertainty of the order of 20%. The images presented in this paper are those obtained with the filtering technique.

Our MeerKAT images of the region between A3562 and SC 1329–313 are shown in the central and lower panel of Fig. 3. The emission at the centre of A3558 is shown in the lower panel of Fig. 4.

3.3. GMRT

The GMRT observations of project 22_039 were pointed on A3558 (see Table 2) and carried out at 306 MHz and 608 MHz, with a bandwidth $\Delta\nu$ = 32 MHz and 256 channels at both frequencies. The LL and RR polarisation were recorded in both bands. The source 1311–222 was used as phase calibrator for both observations, while 3C 286 was used as primary and bandpass calibrator. A standard data reduction approach was carried out. In particular, a-priori calibration, initial flagging, and RFI excision were performed using *flagcal* (Chengalur 2013). Further editing, data averaging, and self-calibration were carried out using the NRAO Astronomical Image Processing System (AIPS). Direction-dependent calibration was successfully carried out at 306 MHz using the task PEELR in AIPS; however, this did not improve the quality of the 608 MHz image, since most of the strong sources in the field are resolved at the resolution of our observations. The final images, covering the full field of the primary beam, were produced over a range of angular resolutions, using different weighting schemes (Briggs parameters robust = 0 and robust = +2) to highlight the details of the more compact features as well as the extended emission in the field. The final images have rms values in the range 60−100 μJy beam^{-1} at 306 MHz and 608 MHz, respectively.

The region of the SC 1329–313 group was observed with the GMRT on May 20 and 21, 2016 (project 30_024) for 2.3 h at 607 MHz and 5.6 h at 233 MHz. Both RR and LL polarisations were recorded. The source 3C 286 was observed at the beginning of each observation as a bandpass and absolute flux density calibrator. The source 1311–222 was observed as a phase calibrator. All data were collected in spectral–line observing mode using the GMRT software correlator. A bandwidth of 33.3 MHz,

Table 3. Logs of the EPIC *XMM-Newton* observations.

OBS-ID	RA (deg)	Dec (deg)	Field name
0105261301	203.26196	−31.665306	A3562_f1
0105261401	202.96821	−31.827528	A3562_f2
0105261501	203.50542	−31.534639	A3562_f3
0105261601	203.13067	−31.652139	A3562_f4
0105261701	203.20183	−31.841722	A3562_f5
0105261801	203.57763	−31.711694	A3562_f6
0107260101	201.97975	−31.479778	A3558
0601980101	202.31887	−31.711917	SC 1327–312a
0601980301	202.38137	−31.477667	SC 1327–312b
0651590101	202.65967	−31.749444	SC 1329–313
0651590201	202.38604	−31.612500	SC 1329–312

512 frequency channels, and a 4 s integration time were used at 607 MHz. At 233 MHz, the bandwidth was 16.7 MHz, divided in 256 channels, and the integration time was set to 8 s. We used the Source Peeling and Atmospheric Modeling (SPAM, Intema et al. 2009) pipeline to reduce the data using a standard calibration scheme consisting of bandpass and gain calibration and subsequent cycles of direction-independent self-calibration, followed by direction-dependent self-calibration. The flux density scale was set using 3C 286 and the Scaife & Heald (2012) scale. For the imaging, the final self-calibrated visibilities were first converted into a measurement set using the Common Astronomy Software Applications (CASA, version 5.6.0) and then imaged using WSClean 2.8. We used the auto-masking and multi-scale algorithms (Offringa & Smirnov 2017) and different values of the Briggs robustness parameter (Briggs 1995), from −0.5 to +0.5, and *uv* tapers. The noise in the final images is of the order of 50 μJy beam^{-1} at 607 MHz and 500 μJy beam^{-1} at 233 MHz. The residual amplitude calibration errors in the GMRT datasets are ∼5% at 607 MHz, ∼8% at 306 MHz, and ∼10% at 233 MHz.

Finally, primary beam correction was applied to all datasets with the task PBCOR in AIPS, following the GMRT guidelines[6]. The full resolution of the final images are 14.0″ × 9.5″ at 306 MHz, 6.3″×3.2″ at 607 MHz and 24.4″×10.7″ at 233 MHz. The primary beam corrected images are shown in the appendix. Our datasets are sensitive to large angular scale emission, ranging from 17′ to 44′.

3.4. XMM-Newton observations

The sky area that covers the four constituents of the central region of the Shapley Supercluster, namely: A3558, A3562, SC 1327–312, SC 1329–313, and their connecting bridges, has been targeted by 11 observations performed with the three European Photon Imaging Cameras (EPIC). For more information, see Table 3.

The surface brightness, and temperature map and profiles presented in this paper (Sects. 4 and 5) have been obtained from the merging of these data sets into a composite event-list.

We sampled this event-list at an angular resolution of 6.5″ and an energy dependent spectral resolution in the range of 15−190 eV. We associated a background noise model to the resulting event cube and an effective area that follow the same angular and spectral sampling. The background noise model includes sky (Cosmic X-ray Background, two component Galactic Transabsorption Emision, see Kuntz & Snowden 2000) and instrumental (soft proton and particle induced) components whose spatial and spectral templates have been jointly normalised with the hot gas emission outside the brightest regions of the Shapley Supercluster core (SSC). Spectral analyses assume a hot gas emission that follows the Astrophysical Plasma Emission Code (APEC, Smith et al. 2001) and an X-ray absorption calibration using an average Galactic neutral hydrogen density column of $N_{\rm HI} = 3.77 \times 10^{20}\,{\rm cm}^{-2}$, which we extracted in the SSC area from a map of the 21 cm emission released by the Leiden/Argentine/Bonn Galactic HI survey (Kalberla et al. 2005).

The surface brightness was obtained with a wavelet analysis of photon images that we corrected for spatial variations of the effective area and background model. Photon images have been denoised via the 4-σ soft-thresholding of variance-stabilised wavelet transforms (Zhang et al. 2008; Starck et al. 2009), which are especially suited to processing low photon counts. The image analyses include the inpainting of detected point-sources and the spatial adaptation of wavelet coefficient thresholds to the spatial variations of the effective area.

We computed the temperature map of the whole field using a spectral-imaging algorithm that combines likelihood estimates of the projected hot gas temperature with a B2-spline wavelet analysis. As detailed in Bourdin & Mazzotta (2008) temperature log-likelihoods are first computed from spectral analyses performed within square bins of various angular resolutions, then convolved with analysis kernels that allows us to derive B2-spline wavelet coefficients and their expected fluctuation. We used such coefficients to derive a wavelet transform that typically analyse projected temperature features of apparent size in the range of $[0.2, 2]$ arcmin, and we reconstructed a denoised temperature map from a 3-σ thresholding of the wavelet coefficients.

4. Radio images and spectral analysis

Figures 3 and 4 clearly show that the central region of the Shapley Supercluster is characterised by several features of diffuse radio emission. Moreover, Fig. 5 shows the diffuse emission in the region between A3562 and SC 1329–313 with the thermal emission detected by *XMM-Newton* overlaid in contours.

Going from east to west we identify (see the labels in the central panel of Fig. 3):

(a) the well-known radio halo in A3562 (V03 and G05);
(b) diffuse emission of very low surface brightness, labelled as ‘arc’ and ‘bridge’, detected here for the first time, which connects the radio halo in A3562 and the radio source J1332–3146a in SC 1329–313;
(c) the diffuse radio source J1332–3146a, first imaged in G05;
(d) a resolved tailed emission just south of J1332–3146a (galaxy SOS 61086) first imaged here;
(e) the head-tail first noticed in V17;
(f) a faint extended emission just south of the head-tail, labelled as ‘bar’;
(g) a diffuse patch of emission 175″ across, of unknown origin, labelled as ‘Southern emisson’;
(h) faint diffuse emission at the centre of A3558, detected for the first time (Fig. 4).

We will describe all these features and provide their observational parameters in the next subsections. Their origin will be discussed in Sect. 5.

[6] www.ncra.tifr.res.in:8081/~ngk/primarybeam/beam.html

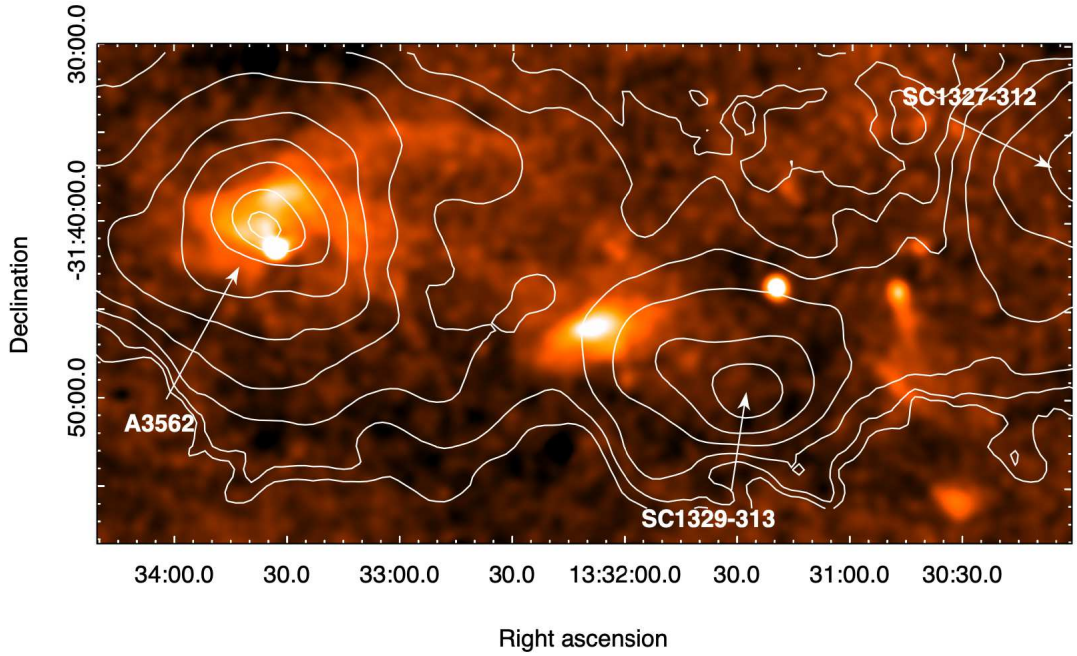

Fig. 5. MeerKAT 1.283 GHz colour scale of the diffuse emission (same field as Fig. 3). The restoring beam is 40″ × 40″. The contours of the *XMM-Newton* surface brightness (see Sect. 3.4) are overlaid in white and are spaced by a factor of 2.

Table 4. Flux density values of the radio halo in A3562.

ν (MHz)	Array	Flux (mJy)	Ref.
1400	VLA	20 ± 2	G05
1283	MeerKAT	26 ± 2	This work
887	ASKAP	48 ± 5	This work
610	GMRT	90 ± 9	G05
332	GMRT	195 ± 39	G05
240	GMRT	220 ± 33	G05

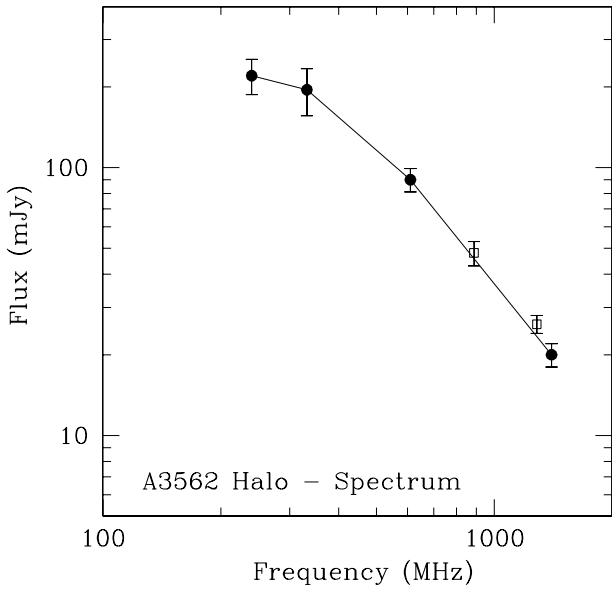

Fig. 6. Radio spectrum of the A3562 radio halo, obtained using the data in Table 4. Filled circles show the data published in V03 and G05, open squares are the new ASKAP and MeerKAT data presented here.

4.1. Radio halo in A3562

The radio halo in A3562 was first imaged with the VLA at 1.4 GHz in V03 and further studied at several radio frequencies and in the X-ray band in G05. With a 1.4 GHz power of 1.14×10^{23} W Hz^{-1}, it is a relatively low-power radio halo, which well fits the radio power–cluster mass correlation for galaxy clusters (Cassano et al. 2013). V03 and G05 reported a spectral index of the order of $\alpha^{1400\,\mathrm{MHz}}_{843\,\mathrm{MHz}} \sim -2$. This value of α is considerably steeper than usually found, that is, $[-1.4, -1.2]$, placing this among the ultra-steep spectrum radio halos, first identified as a particular class of radio halos a few years later in Brunetti et al. (2008).

Our MeerKAT and ASKAP images (Fig. 3) show that this radio halo extends further westwards towards the radio source J1332–3146a in SC 1329–313 (see Sect. 4.3). Its most noticeable new feature is the bright ridge of emission, labelled 'filament' (see Fig. 3, central panel), delimiting the south–eastern edge. Moreover, radio emission is clearly detected for the first time with MeerKAT south of this filament. The surface brightness of the radio halo is of the order of 0.5 μJy arcsec^{-2} and drops to 0.23 μJy arcsec^{-2} in the newly detected region south of the filament. A more detailed analysis of this feature and a revised discussion of the origin of this radio halo will be presented in a separate paper (Giacintucci et al. 2022). Here, in Table 4, we report the flux density measurements of the radio halo, including the new ones, after removal of the embedded point sources. The updated radio spectrum is shown in Fig. 6. The MeerKAT and ASKAP flux density values were obtained integrating over the same area imaged in V03 and G05 for a consistent comparison. The new values perfectly align with the previous measurements and suggest that the spectral index has a value $\alpha^{1283\,\mathrm{MHz}}_{332\,\mathrm{MHz}} = -1.5 \pm 0.2$. The last two datapoints suggest a consistent steepening above 1283 MHz (Giacintucci et al. 2022), in agreement with our earlier work.

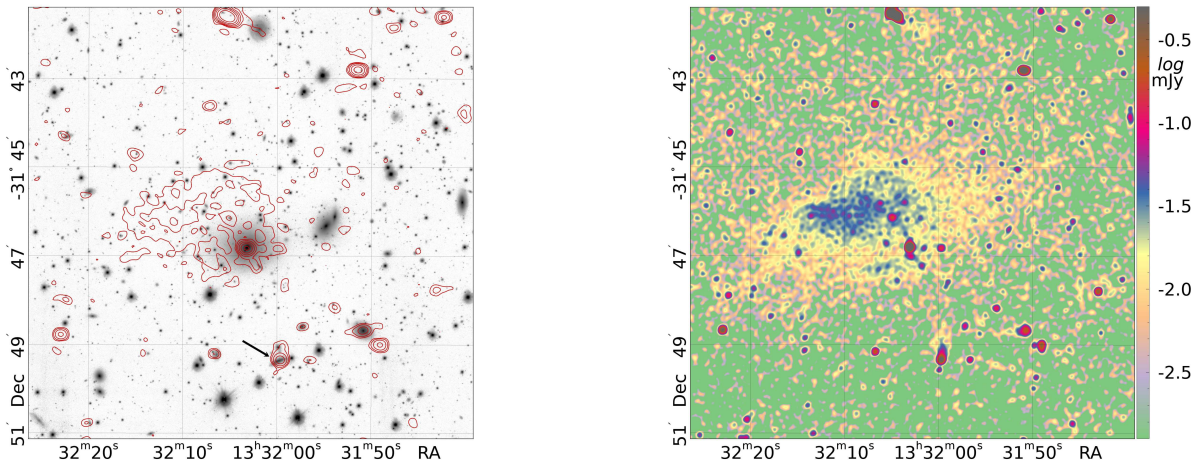

Fig. 7. Contours of the 887 MHz ASKAP image zoomed around J1332–3146a superimposed on the VST *r*-band image (*left panel*). The restoring beam is 13.2″ × 10.4″, p.a. 85.4°. The first contour is drawn at 0.1 mJy beam^{-1}, and the contours are spaced by a factor of 2. SOS 61086, located south of J1332–3146a, is indicated by the black arrow. The first contour is drawn at ∼3σ. Colour scale of the 1.283 GHz MeerKAT image (same as central and bottom panel of Fig. 3), reported to emphasise the structure of the radio emission (*right panel*).

The discovery of the ultra–steep spectrum radio halo in the massive cluster A521 (Brunetti et al. 2008) led to the detection of a number of radio halos with ultra–steep spectrum (see van Weeren et al. 2019 and references therein). It is nowadays thought that such sources are related either to merger events involving clusters of small mass ($M \lesssim 6 \times 10^{14}\ M_{\odot}$) or to off–axis mergers (Cassano et al. 2012). Both the masses of A3562 and SC 1319–313 (see Table 1) and the X-ray properties of this region are consistent with the presence of an ultra–steep spectrum of the radio halo in A3562.

4.2. Diffuse radio emission connecting A3562 and the group SC 1329–313

The most striking result of our observations is the discovery of extended, very low surface-brightness emission in the region connecting A3562 and SC 1329–313, as highlighted in the bottom panels of Figs. 3 and 5. It is the first time that diffuse emission between a cluster and a group is detected at GHz frequencies. Figure 5 shows a remarkable correlation between the morphological details of this feature and the X-ray emission as imaged by *XMM-Newton*.

The possible existence of a radio bridge connecting A3562 and the source J1332–3146a in SC 1329–313 at 1.4 GHz was reported in G05, however, the sensitivity of those observations was not good enough for a robust claim. Similarly, the GMRT observations presented here are not adequate to reveal this feature, due to the pointing centres and limited sensitivity. Our MeerKAT images now clearly detect the radio bridge, which extends from the western end of the radio halo in A3562 (labelled 'filament' in Fig. 9 in G05) to the eastern extension of J1332–3146a, covering a distance of ∼1 Mpc in projection. Moreover, we detect an arc-like feature which connects A3562 and SC 1329–313 from the north. The arc is very well imaged with MeerKAT, while it is less prominent in the ASKAP image, due to the presence of residual ripples (see Sect. 3.1 and Figs. 2 and 3).

We integrated the flux density of this emission over the image presented in the bottom panel of Figs. 3 and 5 after primary beam correction (and removing the contribution of the radio halo in A3562), and obtained $S = 61 \pm 6$ mJy for the total of the diffuse emission (including both the bridge and arc) filling the region between A3562 and J1332–3146a, which corresponds to a radio power $P_{(1.283\,\mathrm{GHz})} = 3.22 \times 10^{23}$ W Hz^{-1}. The average surface brightness is ∼0.09 μJy arcsec^{-2}.

There is strong interest in finding bridges between clusters; they are often not detected, despite high sensitivity (i.e. see the recent ASKAP search of the pre-merger cluster pair A3391–A3395, Brüggen et al. 2021). Successful detections of bridges between cluster pairs have been made using LOFAR at 144 MHz, such as the cluster pair A1758N–A1758S (Botteon et al. 2020a) and the system A399–A401 (Govoni et al. 2019). In addition, there is a well-known bridge connecting the Coma cluster with the NGC 4839 group, detected at 144 MHz (Bonafede et al. 2021) and at 346 MHz (Kim et al. 1989). All these clusters are considerably more massive than A3562 and SC 1329–313, and the detections are well below the GHz frequencies.

4.3. Radio source J1332–3146a

The radio source J1332–3146a was first imaged with the VLA at 1.4 GHz (G05). The source is located just east of the X-ray emission of SC 1329–313 (G05 and Fig. 5). The new ASKAP and MeerKAT images presented here are in very good agreement with the previous ones, but the much better sensitivity and resolution of the current observations provide new insights on the morphology and surface brightness distribution of the emission. The overall size of the source, 6′×2.5′ (∼335×140 kpc), confirms the previous measurement. Figures 3 and 7 clearly show that no jets or other features link the diffuse emission to the compact component, at least at the resolution of our images. We further see no evidence for a connection between the embedded strong compact radio source and the extended emission in the spectral index distribution. The morphology of J1332–3146a is not symmetric with respect to the compact component but extends north and east, with a 1283 MHz (MeerKAT) surface brightness in the range ∼0.14−0.75 μJy arcsec^{-2}.

The embedded bright compact source is located at the southwest end of the radio emission (Fig. 7, left panel) and is associated with a bright early-type galaxy of magnitude[7] $r = 13.56$ with redshift $z = 0.04351$, belonging to

[7] Corrected for Galactic extinction.

SC 1329–313 (Haines et al. 2018). The galaxy (RA_{J2000} = $13^h32^m03.17^s$, Dec_{J2000} = $-31°46'48.5''$) is located along the axis connecting the peaks of the X-ray emission in A3562 and SC 1329–313 (see Figs. 5 and 9 in G05).

We used all the datasets presented here to derive the integrated spectrum, and complemented them with the information published in G05. Table 5 reports the total flux density measurements (after removal of the compact emission associated with the galaxy) and the spectrum is shown in the left panel of Fig. 8. The flux density measurements of J1332–3146a are considerably scattered. The sensitivity of the GMRT 233 MHz observations presented in this paper is too low to detect this source. The 306 MHz flux density value does not align with the data points at higher frequencies and it is not consistent with our previous measurement either. The reason for this discrepancy is unclear. Since the radio source is located at the very edge of the GMRT field of view at this frequency, the local noise is higher and as a consequence the uncertainty on the total flux density is larger than that of the other diffuse sources presented here. If we ignore this measurement, a linear fit to the data provides a value $\alpha^{1283\,\mathrm{MHz}}_{235\,\mathrm{MHz}} = -0.76 \pm 0.2$. A considerable steepening above 1 GHz is suggested by the MeerKAT in-band spectral index image shown in the right panel of Fig. 8 (derived from the $15'' \times 15''$ resolutions images of pointing (d) in SC 1329–313, see Table 2), which covers the frequency range 908−1656 MHz.

The distribution of the in-band spectral index[8] strengthens the idea that the compact radio source and the extended emission are not connected. The former is flat ($\alpha \sim -0.3$ in Fig. 8), while the diffuse emission is considerably steeper, with α in the range $[-2.3, -1]$ across the source. Comparison of the right panel of Figs. 6 and 7 further shows that the region of the diffuse emission where the spectrum is flatter (pink) are those with embedded compact sources, whose spectrum is less steep than the rest. The possible origin of this emission is discussed in Sect. 5.1.1.

4.4. Radio tail of SOS 61086

We identify a tailed radio source south-west of J1332–3146a (Fig. 7, left panel, and Fig. 8, right panel), associated with a spiral galaxy member of SC 1329–313[9] identified as SOS 61086 in the Shapley Optical Survey (Mercurio et al. 2006; Haines et al. 2006). The galaxy has a redshift $z = 0.04261 \pm 0.00023$ (V_h = $12\,500 \pm 70$ km s^{-1}) and is located at ∼280 kpc (∼0.3 r_{200}) in projection from the X-ray centre. Considering the median redshift of SC 1329–313, the line-of-sight peculiar velocity of SOS 61086 with respect to the main group is −900 km s^{-1}. The radio source was detected at 1.4 GHz in Giacintucci et al. (2004) and labelled J1331–3149b; it was classified as unresolved at the resolution and sensitivity of those observations.

The r-band image of the galaxy from the ShaSS (Merluzzi et al. 2015) is shown in Fig. 9 (left panel) superimposed with the contours of the 1.28 GHz MeerKAT image. Because of the hints of matter beyond the galaxy stellar disk in the northerly direction, the object has been investigated in detail with observations carried out with the Wide-Field Spectrograph (Dopita et al. 2007, 2010) mounted at the Nasmyth focus of the Australian National University 2.3 m telescope located at Siding Spring Observatory (Australia), complemented by N-body/hydrodynamical simulations (for the full analysis see Merluzzi et al. 2016). This study demonstrated that the galaxy of stellar mass $\mathcal{M}_\star \sim 4 \times 10^9\,M_\odot$ is undergoing ram-pressure stripping (RPS) and suggested that the time of the onset ('age') of RPS is about 250 Myr ago. Furthermore, the onset epoch estimate agrees with the age of the young stellar population (<200 Myr), suggesting that we are very likely observing ram-pressure-induced star formation.

The new high-quality and deep MeerKAT observations reveal the radio tail, shown in the left panel of Fig. 9. The radio continuum emission peaks at the galaxy centre, and extends north at comparable brightness levels up to 30 kpc in projection from the galaxy disk. The other striking feature of the radio continuum emission is its confinement to the inner part of the disk which recalls the truncation of the gas disk in galaxies affected by RPS.

We used our images to derive the spectrum of the radio emission associated with the galaxy disk and that of the tail, which are shown in the right panel of Fig. 9. The spectrum of the tail (computed using images at similar angular resolution) is considerably steeper than the emission from the galaxy and it is very well fit by a power law with $\alpha^{1283\,\mathrm{MHz}}_{306\,\mathrm{MHz}} = -0.79 \pm 0.05$. The flux density values of the disk are more scattered, and this could be partly due to the different resolutions of the images. We further note that the MeerKAT in-band spectral index of SOS 61086, shown in the inset of the right panel of Fig. 8, clearly shows a steepening along the tail, up to $\alpha \sim -2$. Assuming that the spectrum of the tail steepens above ∼1.2 GHz, as suggested from the in-band spectral index, we derive a magnetic field $H_{eq} = 0.9\,\mu$G, and an upper limit to the radiative age of the relativistic electrons of ∼100 Myr (including the aging of the electrons due to scattering with the CMB). Finally, Figs. 5 and 7 (right panel) suggest that a much fainter diffuse intercluster radio emission extends north of SOS 61086 to J1332–3146a, over an extent of ∼90 kpc.

Table 5. Flux density values of J1332–3146a.

ν (MHz)	Array	Flux (mJy)	Ref.
1400	VLA	16 ± 1	G05
1283	MeerKAT	18 ± 2	This work
887	ASKAP	28 ± 2	This work
610	GMRT	28 ± 3	G05
607 [(a)]	GMRT	32 ± 2	This work
306 [(b)]	GMRT	152 ± 39	This work
330	GMRT	56 ± 6	G05
235	GMRT	89 ± 10	G05

Notes. [(a)]Project 30_024 and [(b)]Project 22_039 in Table 2.

[8] To fit the in-band spectral indices, we used a new spectral fitting code (part of the PFB-Clean) (https://github.com/ratt-ru/pfb-clean). This proceeds as follows. The per-subband (8, in this case) model and residual images produced by wsclean are reconvolved to a common resolution. A power law is then fitted pixel-by-pixel (weighting the subbands as per the "wsum" FITS keyword generated by wsclean). The subband images are generated by the same run of wsclean as the MFS image, and use a weighting of robust = 0 (without the "use MFS weighting" option of wsclean in effect, so the weighting is truly robust = 0 per subband). The primary beam is accounted for by directly incorporating attenuation by the average Stokes I beam into spectral index model during the fitting. We used the Eidos beam model (https://github.com/ratt-ru/eidos) (Asad et al. 2021 in this particular instance).

[9] The membership has been statistically assigned by means of the dynamical analysis in Haines et al. (2018).

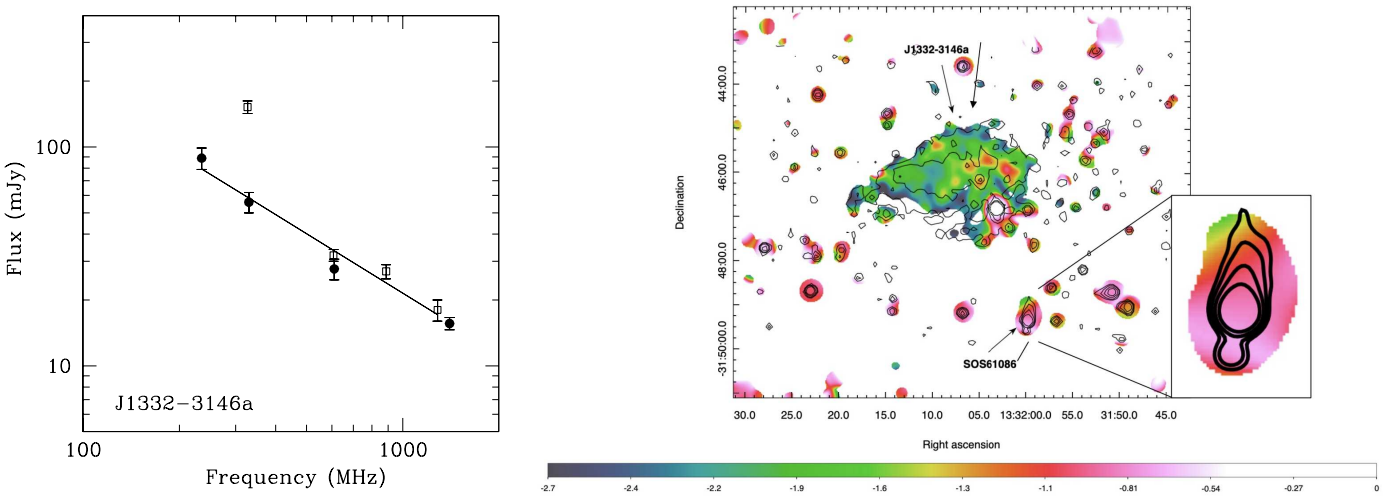

Fig. 8. Radio spectrum of the radio source J1332–3146a, obtained using the data in Table 5 (*left panel*). Filled dots are from G05, open squares are from the present paper. The fit does not include the 306 MHz measurement (see Sect. 4.3). In-band MeerKAT spectral image at the resolution of $15'' \times 15''$ (*right panel*). The radio contours are from the full resolution image, i.e. $7.3'' \times 7.2''$, and are drawn at ±20, 40, 80, and 160 μJy beam^{-1}. A zoom of the radio source associated with SOS 61086 is shown in the inset.

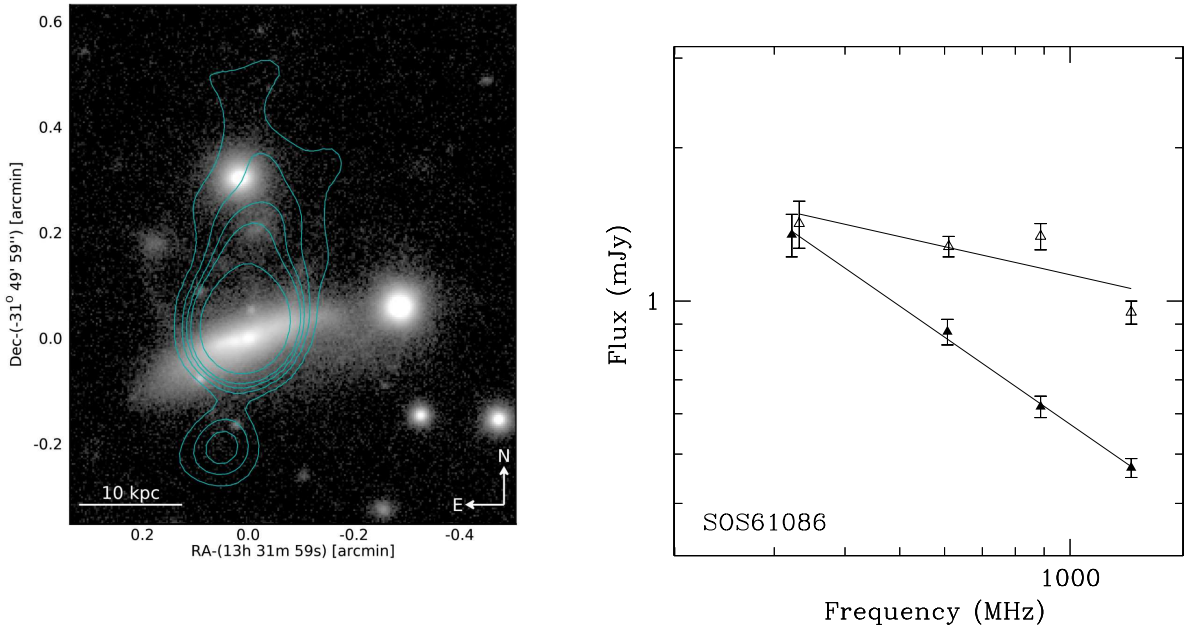

Fig. 9. ESO-VST *r*-band image of the field including SOS 61086 with 1.28 GHz MeerKAT radio contours superposed (*left panel*). The restoring beam of the radio image is $6.9'' \times 6.5''$, p.a. 151.8°. The contours are plotted at 20, 40, 60, 160 μJy beam^{-1}. The first contour is drawn at ~3.5σ (the local noise is ~6 μJy beam^{-1}). The scales (RA and Dec) give the distance (in arcsec) from the photometric centre of the galaxy. Spectrum of the radio emission of SOS 61086 (*right panel*). Open and filled triangles are the emission from the galaxy and the tail, respectively.

Table 6. Flux density values of the head-tail and southern feature.

ν (MHz)	Array	Resolution ($'' \times ''$)	Core+ Inner tail (mJy)	Broken tail (mJy)	Bar (mJy)	Southern emission (mJy)
1283	MeerKAT	7.66×7.26	8.3 ± 0.4	4.8 ± 0.2	2.5 ± 0.1	3.7 ± 0.1
887	ASKAP	13.23×10.43	11.3 ± 0.6	7.0 ± 0.4	5.3 ± 0.3	4.0 ± 0.2
607 [(a)]	GMRT	9.73×5.55	11.5 ± 0.6	9.5 ± 0.5	10.3 ± 0.5	–
607 [(a)]	GMRT	15×15	12.8 ± 0.6	10.9 ± 0.5	10.7 ± 0.5	4.8 ± 0.2
306 [(b)]	GMRT	14.05×9.53	17.6 ± 1.4	42.3 ± 3.4	42.2 ± 3.4	–
233	GMRT	24.45×10.77	15.2 ± 1.5	–	38.0 ± 3.8	–

Notes. [(a)]Project 30_024 and [(b)]Project 22_039 in Table 2.

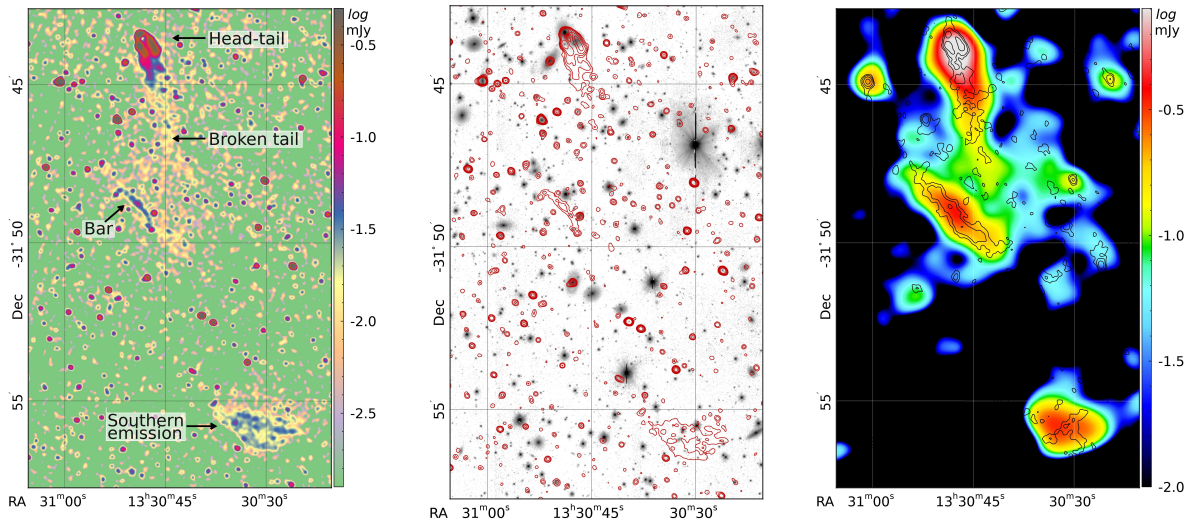

Fig. 10. 1.283 GHz MeerKAT image of the head-tail in SC J1329–313 (*left panel*). The colour scale is in the range −1 to 0.1 mJy beam^{-1}. The restoring beam of the image is 7.66″ × 7.28″, in p.a. 68°. The various features of diffuse emission are indicated. Contours of the same image overlaid on the ESO-VST *r*-band image (*central panel*). The contour levels are ±20, 40, 80, 160 µJy beam^{-1}. The first contour corresponds to ∼3σ. *Right panel*: 1.283 GHz MeerKAT image of the diffuse emission at the resolution of 40″ × 40″ in colour with GMRT contours at 306 MHz overlaid. The contours are drawn at 0.2, 0.4, 0.8 mJy beam^{-1}. The angular resolution is 14.0″ × 9.5″.

4.5. Head–tail in SC 1329–313

The ASKAP and MeerKAT images in Fig. 3 show an intriguing emission west of J1332–3146a, at RA ∼ 13^{h}30^{m}40^{s}. A zoom into that area is given in Fig. 10.

The head–tail radio source is associated with a cluster galaxy located at RA$_{J2000}$ = 13^{h}30^{m}48.91^{s}, Dec$_{J2000}$ = 31°43′25.6″, with z = 0.044 and magnitude R = 13.6 (from the NASA/IPAC Extragalactic Database). However, a superimposed foreground star makes the magnitude measurement unreliable. The galaxy and the star can be distinguished only in the VISTA K-band image of ShaSS. The two jets of the tail bend sharply just outside the envelope of the optical galaxy, and lose their collimation at a distance of ∼40 kpc from the core, to form a feature of very low surface brightness emission, which we refer to as the broken tail, extending ∼250 kpc southwards. At that location the morphology of the emission changes again, to take the shape of a bar inclined at ∼30° with respect to the orientation of the broken tail. The length of the bar is ∼250 kpc. Part of this emission was detected with the GMRT at 306 MHz (V17), however, the sensitivity of those observations did not allow for a clear morphological classification of the source.

Table 6 reports the flux density of all these components in our datasets. At 1283 MHz, we considered the values derived from the MGCLS (pointing (d) in Table 2) to avoid any possible uncertainties in the primary beam correction at very large distance from the pointing centre. At 607 MHz we reported the values at different resolutions to ensure the full detection of the extended features. Only the inner part of the tail and the bar are detected at 233 MHz. One possibility is that the core is self-absorbed at frequencies below 306 MHz, while the broken tail and the southern emission most likely fall below the sensitivity limit of those observations. All the remaining features are clearly detected in all datasets.

The spectra of the various features are shown in the left and right panels of Fig. 11. The spectrum shown in the left panel includes both the core and the inner part of the head-tail, corresponding to the red area in the left panel of Fig. 10. The irregular trend is most likely the result of the different components in the core and jets, which are difficult to disentangle. Overall this region shows an approximately flat spectrum. The situation is completely different in the broken tail and in the bar. Both features are steep, and a linear fit provides $\alpha^{1283\,\mathrm{MHz}}_{306\,\mathrm{MHz}} = -1.0 \pm 0.1$ in the broken tail, and $\alpha^{1283\,\mathrm{MHz}}_{306\,\mathrm{MHz}} = -1.95 \pm 0.05$ in the bar.

The spectral index values of the various features are confirmed by the MeerKAT spectral index image shown in the left panel of Fig. 12 (derived from pointing (b) in SC 1329–313, see Table 2). The core of the head–tail has a spectral index $\alpha \sim -0.5$, with a clear steepening along the jets, and the remarkable steepness of the bar is confirmed, with $\alpha \lesssim -2$.

We used the pointing from the MGCLS (see Table 2) to search for polarisation information on the head-tail and the bar. Preliminary Q and U images from the MGCLS were constructed by summing the respective individual frequency channels and, thus, they do not correct for any Faraday rotation, spectral index, or depolarisation effects. The approximate fractional polarisations are shown in the right panel of Fig. 12. With the above caveats, the observed fractional polarisation is most prominent in the eastern tail, and increases from values of the order of 10% near the core to an approximate level of 70%, which is the theoretical maximum, for the bar. More precise results would require a full Faraday synthesis, which is beyond the scope of the current work.

4.6. Southern emission

This interesting feature is not obviously connected to any optical source, as is clear from the central panel of Fig. 10. The surface brightness is quite uniform and its spectrum, with $\alpha^{1283\,\mathrm{MHz}}_{607\,\mathrm{MHz}} = -0.35 \pm 0.12$, is unusually flat for diffuse sources with no optical counterpart. Figure 5 shows that it is outside the region covered by the *XMM-Newton* observations.

These properties challenge its classification within the current classes of extragalactic radio sources. Assuming that the source is located at the distance of the Shapley Supercluster, its size is ∼167 × 83 kpc. The source is too faint to allow in-band spectral imaging.

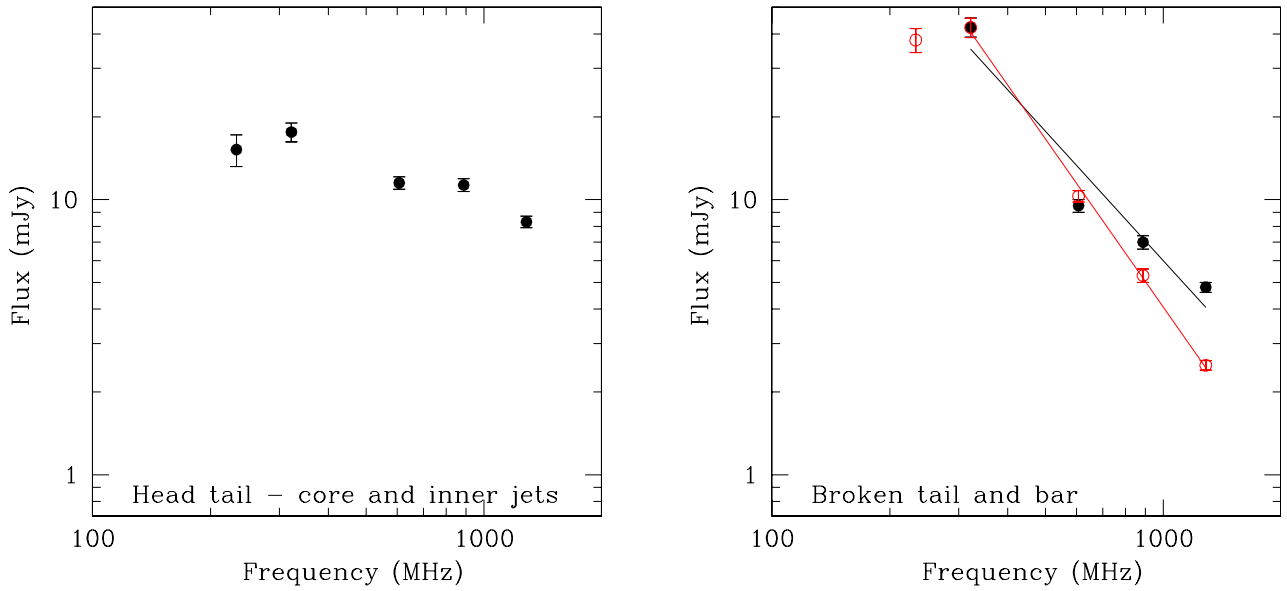

Fig. 11. Spectra of the components in the head–tail radio galaxy. *Left panel*: core region, encompassing the core and the inner tail (red area in the left panel of Fig. 10). *Right panel*: broken tail (black filled circles) and bar (red open circles).

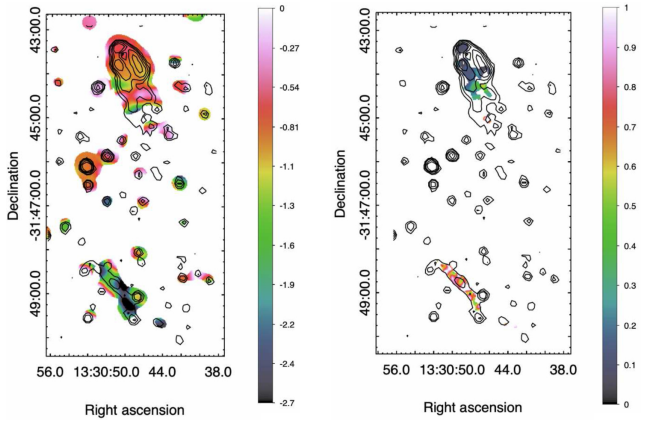

Fig. 12. MeerKAT 1–1.8 GHz in-band spectral image of the head-tail, broken tail, and bar at the resolution of $15'' \times 15''$ (*left panel*). Contours are the same as in the central panel of Fig. 10. *Right panel*: same contours as in the left panel overlaid on the fractional polarisation shown in colour.

We note that the brightest optical/infrared object co-located with the southern emission is a giant star (WISEA J133029.79, *Gaia* 6169476948, Stassun et al. 2019) with a high proper motion (-4.72 ± 0.05 mas yr^{-1} in RA and -2.41 ± 0.04 mas yr^{-1} in Dec). At a distance of 3850 ± 400 pc, this corresponds to a velocity of $\sim$100 km s^{-1}. If the flat-spectrum southern emission were associated with this star, it would have a size of $\sim 4 \times 2.5$ pc, and a 1 GHz monochromatic luminosity of 6.4×10^{12} W Hz^{-1}. For comparison, this is 40 times the surface area and 10 times the luminosity of the optically thin free-free emission from the outer portion of the mass loss wind from P Cygni (Skinner et al. 1998).

4.7. Diffuse emission at the centre of A3558

A3558 is located $\sim$2.8 Mpc west of SC 1329–313 and is the most massive cluster in the Shapley Supercluster (Table 1). Its size and overall dynamical state as derived from the X-ray properties (Rossetti et al. 2007) make it an ideal candidate to host diffuse emission in the form of a radio halo, undetected prior to our observations.

Diffuse emission was detected with both ASKAP and MeerKAT. The ASKAP contours of the diffuse emission are shown in the upper panel of Fig. 13 overlaid on the [0.5, 2.5]-keV emission imaged by *XMM-Newton*. The lower panel shows the MeerKAT contours overlaid on the *XMM-Newton* pseudo-entropy map (see Sect. 5.1.3). The source subtraction in the ASKAP image was carried out using the task SAD in AIPS, down to 0.3 mJy, and the residuals were convolved with a beam of $25.1'' \times 20.9''$. This subtraction provided cleaner results in this region than the compact source subtraction methods used earlier. Some residuals are present beyond the bulk of the diffuse emission, however, it is difficult to say whether they are the result of incomplete source subtraction or an indication that the halo could be more extended. The MeerKAT emission was imaged after subtraction of the individual radio sources in the u–v plane, and the residuals were convolved to a resolution of $40.9'' \times 40.4''$. Our 306 MHz and 608 MHz GMRT observations, although they are pointed on the cluster centre, are not sensitive enough to detect this very faint source.

The extent of the diffuse emission is consistent at 887 MHz and at 1.28 GHz, that is, $\sim$400×200 kpc, and its major axis points towards the small group SC 1327–312. The overall shape and size of this structure are consistent with the brightest region of X-ray emission as detected by *XMM-Newton* (Rossetti et al. 2007), as discussed in Sect. 5.

We measure a flux density $S_{887\,\mathrm{MHz}} = 30 \pm 3$ mJy and $S_{1283\,\mathrm{MHz}} = 13 \pm 1$ mJy, which lead to a very steep spectrum, $\alpha^{1283\,\mathrm{MHz}}_{887\,\mathrm{MHz}} = -2.3 \pm 0.4$. The surface brightness at 1.283 GHz is very low, that is, $\sim$0.1 μJy arcesc^{-2}. The corresponding radio powers are $P_{887\,\mathrm{MHz}} = 1.58 \times 10^{23}$ W Hz^{-1} and $P_{1283\,\mathrm{MHz}} = 6.85 \times 10^{22}$ W Hz^{-1}.

5. Discussion

The ongoing merging and accretion processes in the A3558 complex are supported by observational evidence over the full

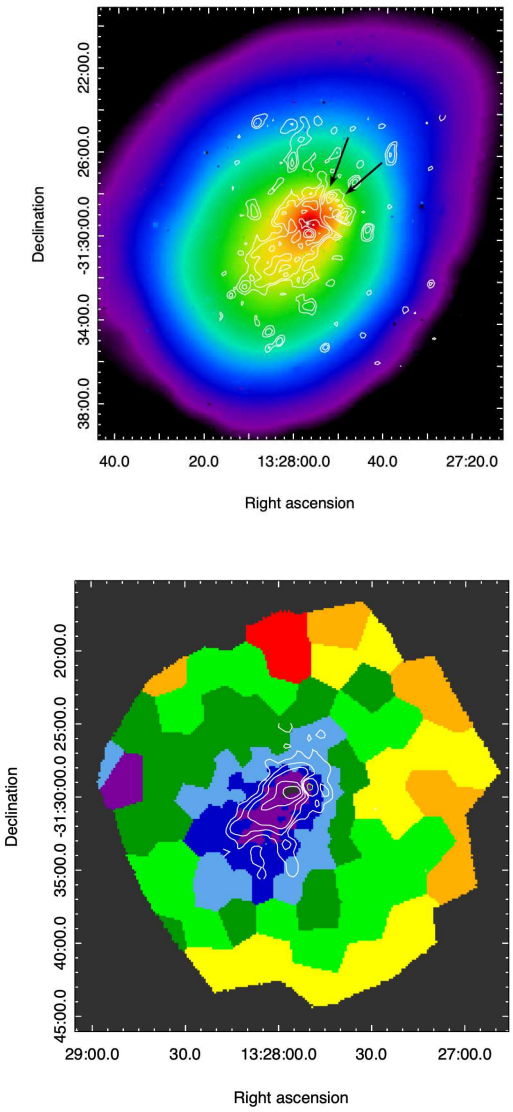

Fig. 13. Radio halo in A3558. *Upper panel*: ASKAP 887 MHz contours (after subtraction of the embedded individual sources; see Sect. 4.7) overlaid on the [0.5, 2.5]-keV *XMM-Newton* image (Rossetti et al. 2007). The resolution is 25.1″ × 20.9″, in p.a. 131.5°, and the rms is ∼35 μJy beam^{-1}. Contour levels start at ±0.15 mJy beam^{-1} and are spaced by $\sqrt{2}$. The location of the cold front is indicated by the black arrows. *Lower panel*: MeerKAT 1.283 GHz contours after subtraction of the point sources and convolution with a restoring beam of 40.9″ × 40.4″, in p.a. 144.6°, overlaid on the pseudo-entropy (expressed in arbitrary units) obtained from the *XMM-Newton* observations (Rossetti et al. 2007). Purple and blue show low pseudo-entropy regions. The rms is ∼35 μJy beam^{-1}. Contour levels start at ±0.125 mJy beam^{-1} and are spaced by $\sqrt{2}$.

spectrum, from the radio to the X-ray, however, their respective details are difficult to disentangle.

Thanks to the unprecedented quality of the radio images presented here, seamlessly covering the frequency range from 0.23 to 1.65 GHz, with the MeerKAT images reaching μJy beam^{-1} sensitivity at GHz frequencies over a wide range of angular scales, from few arcsec to approximately 10′, our new findings are adding important pieces of information to the details of accretion and merging in the supercluster core.

5.1. Insights from the comparison of the non–thermal and thermal properties

On the basis of a deep analysis based on *XMM-Newton* and *Chandra* data, Rossetti et al. (2007) classified A3558 as an intermediate case between cool-core and non cool-core cluster (consistent with the later classification of Hudson et al. 2010) and argued that most likely the relaxation process of the cluster has been perturbed either by the passage of the small group SC 1327–312, or by an off-axis merger with a more massive cluster, whose debris are A3562 and the two SC groups in the region between A3558 and A3562. Finoguenov et al. (2004) explained the thermal properties of A3562 as due to sloshing induced by the passage of the group SC 1329–313 north of A3562 itself, coming from east and directed westwards. This is supported by the presence of the ultra-steep spectrum radio halo in A3562, whose origin was explained as the result of particle re-acceleration induced by turbulence injected in the ICM by the passage of SC 1329–313 north of the core of A3562 and by the oscillation of the cluster core (sloshing) in the north-south direction (G05). In the following, we discuss the origin of the various features presented in this paper, going from east (A3562) to west (A3558), informed by the comparison of X-ray and radio emission as seen in Figs. 5, 13, and 14.

5.1.1. Region between A3562 and SC 1329–313

Figure 5 shows a tight correspondence between the radio and X-ray emission in the whole region going from the centre of A3562 and SC 1329–313. Beyond the new detection of the arc, both with MeerKAT and *XMM-Newton*, from the figure it is clear that the end part of the radio arc (in the west direction) and the bridge connecting A3562 and J1332–3146a are located in the plateau of X-ray emission connecting A3562 and SC 1329–313. Finally, the temperature map shown in Fig. 14 has an enhancement in the region between A3562 and SC 1329–313. From Table 1, we infer a mass ratio of ∼1:9 between SC 1329–313 and A3562, namely, we are in the minor merger frame.

The remarkable coincidence of the arc with a similar feature in the X-ray emission lends strong support to the hypothesis made in Finoguenov et al. (2004) that SC 1329–313 has come from the east, travelling north of A3562 and then is deflected south to reach its current position. Such a passage may have induced the sloshing at the origin of the radio halo in A3562, as proposed in G05, and injected very mild turbulence in the ICM responsible for the extremely low surface brightness emission of the arc and the bridge.

The observed properties of the radio source J1332–3146a are consistent with a merger scenario. On one hand, we see no evidence of a connection between this diffuse source and the compact radio source associated with the bright member of SC 1329–313, that is, no radio jets are present at the resolution of our images and the spectral index distribution shows a sharp transition between these two features (see right panel of Fig. 8). On the other hand, the electrons responsible for the diffuse emission may have been deposited in the ICM in a previous cycle of radio activity of the same galaxy and re-accelerated by the turbulence injected in this region by the flyby of SC 1329–313. The steep spectrum of this source and the distribution of the MeerKAT in-band spectral index are consistent with a re-acceleration origin. We note that the fan-like morphology of the radio halo in A3562 and of J1332–3146a, opening up towards the north, seems to suggest that the source of the perturbation comes from the north.

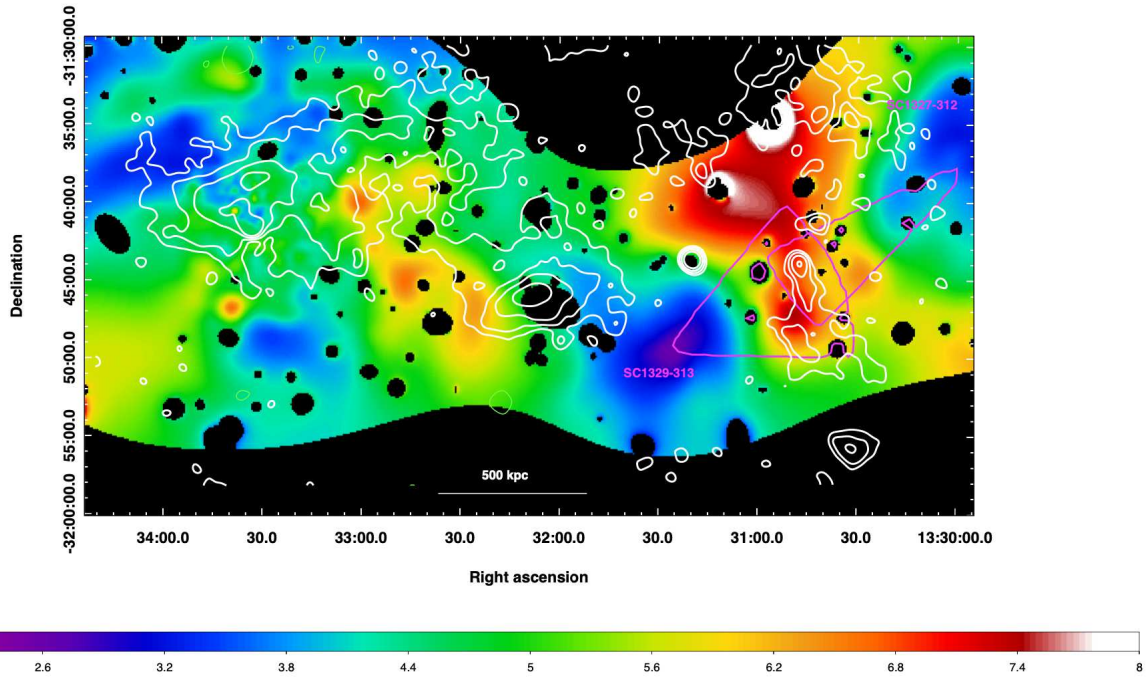

Fig. 14. [0.3, 12]-keV *XMM-Newton* temperature map (in colour) computed from wavelet spectral-imaging (see Sect. 3.4). Contours of the MeerKAT 1.28 GHz image at the resolution of 40″ × 40″ (same as bottom panel of Fig. 3) are overlaid in white. The contours are drawn at ±0.1, 0.2, 0.4, 0.8 mJy beam^{-1}. The average rms in the image is ∼30 μJy beam^{-1}. The black areas are the subtracted individual sources. The magenta sectors show the regions of extraction of the temperature profiles in SC 1327–312 and SC 1329–313 (Sect. 5.2 and Fig. 15).

Alternatively, the location of J1332–3146a just at the edge of the X-ray emission of J1329–313 (see Fig. 5) opens the possibility of a relic-type source. The polarisation information, which is not available at present, would be highly valuable with regard to completing the picture of the possible origin of this source.

We estimated the equipartition magnetic field in the arc and bridge between A3562 and SC 1329–313, assuming a cylindrical geometry for the region of emission and we obtained $H_{\rm eq} \sim 0.78\,\mu$G. This value is very close to the assumption made in G05 to estimate the strength of the fluid turbulence injected in the ICM in the merger scenario considered here. As postulated in G05, our results clearly show that indeed the western extension of the radio halo in A3562 and J1332–3146a are the peaks of a much more extended emission, which are finally detectable with the current generation of radio interferometers.

Since this emission has thus far only been detected at 1.283 GHz, its spectrum is not yet known. Under the assumption of a spectral break between 0.6 and 1.4 GHz, the corresponding radiative age of the relativistic electrons responsible for the radio emission ranges from ∼132 Myr to 86 Myr (accounting for the losses of the electrons due to the scattering with the cosmic microwave background field $H_{\rm CMB}$). Such values are considerably lower than the estimated age of the interaction between A3562 and SC 1329–313 (∼1 Gyr, see Finoguenov et al. 2004), implying that turbulence has to be active now.

5.1.2. Region between the two groups SC 1329–313 and SC 1327–312

The X-ray properties of these two groups were studied with *Beppo*–SAX (Bardelli et al. 2002). No shocks were detected in either of them, which led the authors to suggest a late merger for the whole structure under study here.

Figures 5 and 14 clearly show that the head-tail is located exactly in the bridge of emission connecting the two SC groups, where a temperature enhancement is detected, reaching values of the order of 7–7.5 keV, the highest in the region under investigation. We estimated the significance of this enhancement compared to SC 1327–312 and SC 1329–313 by extracting the temperature profile along the sectors shown in magenta in Fig. 14 over five bins in each sector. The result is shown in Fig. 15, with the errorbars corresponding to 1σ. The significance of the enhancement in the region where the head-tail is located is above 2σ. Unfortunately, the exposure of the X-ray observations is not deep enough to search for discontinuities in this low surface brightness region.

The combination of this high temperature and the high fractional polarisation in the eastern part of the tail, particularly in the bar (right panel in Fig. 12) are, again, suggestive of interaction between the radio plasma and some discontinuity.

Tails with bars like the one detected here are being detected in other clusters, such as Ophiuchus (Giacintucci et al. 2022) and A2443 (Cohen & Clarke 2011). The morphology and spectral trend (the spectrum steepening towards the bar, which is the steepest feature) for our source bear close similarities to simulations of interactions between radio galaxies and cluster shocks propagating perpendicular to the radio jet axis (Nolting et al. 2019). The polarisation properties and the ordered magnetic field which we find would be consistent with this scenario. The shocks (Nolting et al. 2019) used in their simulations have Mach numbers in the range between 2–4. Such strong shocks have not generally been expected in the peripheral regions of a supercluster, but they might be an example of the 'runaway' shocks proposed by Zhang et al. (2019), which maintain their strengths in regions with steep density gradients.

The southern emission (Sect. 4.6) lies outside the region covered by the *XMM-Newton* observations, as is clear also from

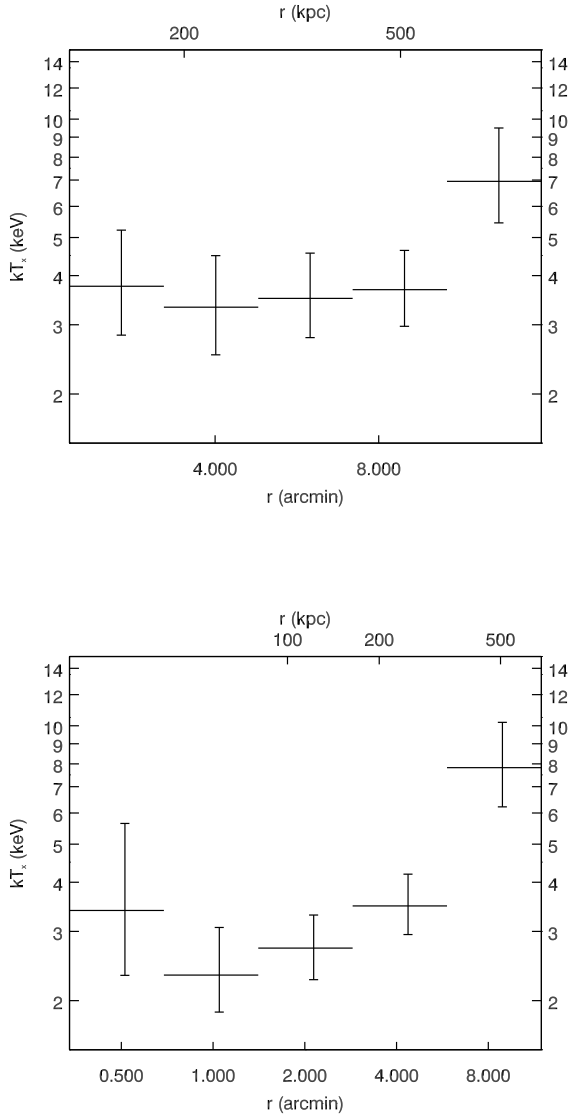

Fig. 15. Temperature profiles derived from the sectors shown in Fig. 14 for SC 1327–312 (*upper panel*) and SC 1329–313 (*lower panel*).

Figs. 5 and 14. This does not allow any further classification or speculation on its origin.

5.1.3. Diffuse emission at the centre of A3558

The upper panel of Fig. 13 clearly shows that the diffuse source at the centre of A3558 is perfectly coincident with the brightest part of the X-ray emission as imaged by *XMM-Newton*.

A3558 is an intriguing cluster. Based on the analysis of *XMM-Newton* and *Chandra* observations, Rossetti et al. (2007) concluded that the cluster has properties both of cool-core and merging clusters, with a cold front in the north-western edge (whose position is shown in the upper panel of Fig. 13) and a low entropy tail (shown in colour in the lower panel of Fig. 13), but with an overall lack of central symmetry in its thermal properties. A multi-wavelength study of the brightest cluster galaxies (BCG) in the core of the Shapley Supercluster (Di Gennaro et al. 2018) reports that the BCG in A3558 has radio properties that are similar to those in merging clusters. The diffuse radio emission detected at its centre (Sect. 4.7) reflects this anomalous situation. The extent of the radio emission is smaller than typical radio halos (~400 × 200 kpc), and its power, $P_{1.283\,\mathrm{GHz}} = 6.85 \times 10^{22}$ W Hz^{-1}, is very low. If we consider the value of M_{500} given in Table 1 and scale the radio power to 1.4 GHz using the spectral index obtained here ($\alpha = -2.3$), we see that this this emission is extremely underluminous compared to what is expected from the M_{500}–$P_{1.4\,\mathrm{GHz}}$ correlation for radio halos (i.e. Cuciti et al. 2021; Duchesne et al. 2021a). On the other hand, the emission is in reasonable agreement with the L_X–$P_{1.4\,\mathrm{GHz}}$ correlation for mini-halos (Kale et al. 2015). We note that its north-western boundary is coincident with the cold front detected in Rossetti et al. (2007) and highlighted in the upper panel of Fig. 13, and the overall emission is aligned along the bright ridge of X-ray emission. This region corresponds to the low-entropy tail (see lower panel of Fig. 13).

Rossetti et al. (2007) explained the thermal properties of A3558 as due to sloshing induced by a perturber, most likely SC 1327–312. The underluminous very steep spectrum of the diffuse emission in A3558 is consistent with the possibility that the origin of this source is sloshing induced by a minor merger, the mass ratio between SC 1327–312 and A3558 being ~1:5. The case of A3558 is reminiscent of A2142, another cluster with intermediate properties between cool-core and non-cool-core clusters (Rossetti et al. 2013) where large-scale sloshing was invoked to account for the origin of the two-component Mpc-scale radio halo (Venturi et al. 2017b).

Whether this is a radio halo or a mini-halo remains unclear, and this sharp classification is probably inadequate to reflect the complexity of the Shapley Supercluster core and of the relation between radio halos and cluster mergers at a more general level. This is also shown in Savini et al. (2019), where large-scale radio emission in the form of radio halos in non-merging clusters has been detected at low frequencies.

5.2. Origin of the radio tail of SOS 61086

A fundamental piece of evidence of the ongoing RPS affecting the galaxy SOS 61086 has been provided by the distribution of the Hα emission derived from IFS and shown in Fig. 16. The IFS data indicate that ionised gas spreads out from the disk of the galaxy in a sort of triangular region, with a vertex in the central disk and one side at ~16 kpc north and directed approximately E–W with clumps of gas extending further in the north, reaching about 30 kpc in projection. The gas disk appears clearly truncated beyond ~6 kpc from the centre along the major axis. A possible interaction with the other member of SC 1329–313 located approximately 17 kpc north of SOS 61086 (see left panel of Fig. 9) has been excluded considering the lack of any sign of perturbation in the stellar disk of this 'red and dead' galaxy, as well as the shape and extent of the ionised gas tail going beyond the northern galaxy in projection.

In SOS 61086, the radio-emitting plasma and the ionised gas show equal extent in projection from the galaxy disk (see Fig. 16), although the ionised gas tail is wider (~28 kpc E–W wide at ~16 kpc North of the disk) and it looks fragmented into clumps in the section farthest from the disk. We note that the Hα flux in Fig. 16 is above 5σ level[10] almost everywhere, and the first radio continuum contour in the tail corresponds to ~3.5 times the local noise. In addition, the two emissions overlap in the galaxy disk, suggesting that the ram pressure causing the truncation of the gas disk affects the radio-emitting plasma with

[10] The sensitivity of the IFS observations was 0.5 × 10^{-17} erg cm^{-2} s^{-1} arcsec^{-2} at a signal-to-noise ratio SNR = 5 for the Hα line (Merluzzi et al. 2016).

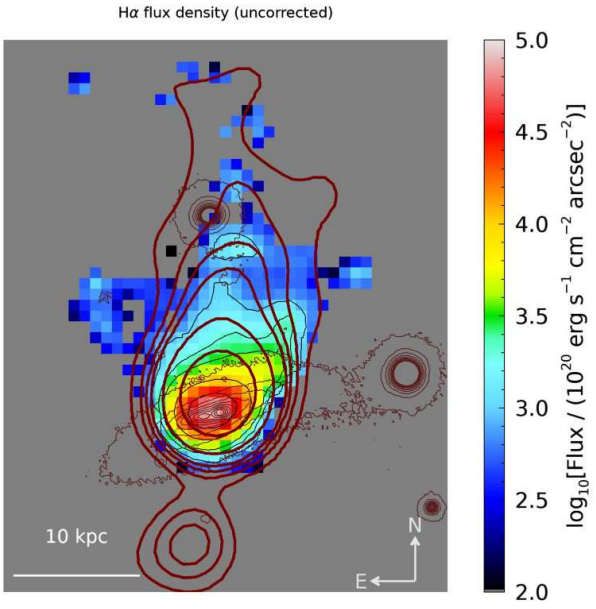

Fig. 16. Hα flux for SOS 61086 derived from IFS data. The *r*-band contours and the MeerKAT radio contours (same as Fig. 9, left panel) are shown in thin and thick red lines, respectively.

similar efficiency. Therefore, we can confirm that, at our sensitivity, the magnetic field and the warm ionised gas traced by the Hα emission are closely linked, in agreement with what is observed in the Virgo galaxy NGC 4438 (Vollmer et al. 2009).

Ram-pressure stripped tails detected in radio continuum have been identified and analyzed in the Virgo cluster (Vollmer et al. 2004, 2009), the Coma cluster (Crowl et al. 2005) and Abell 1367 (see Gavazzi et al. 1995 and references therein). Recently, Chen et al. (2020) carried out a 1.4 GHz continuum and HI emission survey in the Coma cluster to investigate the radio properties of RPS galaxies. They detected radio continuum tails in 50% of the targets demonstrating the widespread presence of relativistic electrons and magnetic fields in the stripped tails. Now, the origin of the radio continuum emission in the tail of each RPS galaxy is under debate, assumed to be possibly related either to 'in situ' star formation (Gavazzi et al. 1995 and references therein) or to relativistic electrons stripped from the galaxy by ram pressure and possibly re-accelerated (i.e. Chen et al. 2020). In order to distinguish and quantify these two contributions, multi-band data are mandatory, as shown in the above studies. This approach is also essential since different physical processes may contribute to the emission at each wavelength. The ionised gas as traced by the Hα radiation, for instance, can be photoionised in the HII regions, namely, it maps the youngest stellar population, or it may be shock-ionised in the turbulent tail by the ram pressure (i.e. Merluzzi et al. 2013).

5.3. Multi-band analysis of the galaxy extraplanar emission

Beside the morphological conformity, for SOS 61068 the other pieces of evidence supporting a scenario where the radio-emitting plasma and warm gas tails originate from the same mechanism, that is, RPS, is given by the consistency (see Sect. 4.4 and references therein) among the epoch of the onset of stripping (~250 Myr), the age of the youngest stellar population (<200 Myr), and the age of the radio tail (~100 Myr).

For SOS 61086, the line ratios observed in the ionised gas indicate that it is mainly photoionised by hot stars, both in the galaxy disk and in the tail, and that shocks are important in determining the excitation only in a NE region of the tail. The integrated Hα-derived star formation rate (SFR) of SOS 61086, excluding the contribution of the shock-ionised gas, amounts to $1.8 \pm 0.6\, M_{\odot}\, \mathrm{yr}^{-1}$, half of which occurs in a central region of 2.5 kpc radius (Merluzzi et al. 2016) and with lower star formation in the detached gas. Haines et al. (2011) derived the relation between the SFR and the 1.4 GHz flux for the Shapley galaxies. Considering the SFR and the measured 1.4 GHz flux of SOS 61086 (1.34 mJy), the galaxy follows the sequence of the star-forming spiral galaxies and does not show any radio excess (see Fig. 5 of Haines et al. 2011).

All together, this evidence points towards a common cause of the radio and Hα tails, but does not enable us to disentangle the origin of the relativistic electrons in the tail. The relative lengths and strength of the radio continuum emission and the Hα extraplanar tails may help in this investigation. Gavazzi et al. (1995) observed two cases where the radio tail significantly exceeds the Hα one in projection. By contrast, the radio continuum tails detected in the RPS galaxies of the Coma cluster by Chen et al. (2020) are usually shorter than the Hα tails. Of course, these differences in the relative extents of the radio and Hα tails can be explained with differences in sensitivities among the studies, but with respect to our data and those of Chen et al. (2020), this seems not to be the case. Both radio observations and Hα fluxes reach comparable depths and the projected lengths of the radio and Hα tails are similar. Considering the age estimated for the relativistic electrons (≤100 Myr) and the projected length of the tail (~30 kpc) we obtain a velocity of the gas stripped from the galaxy of $\sim 300\, \mathrm{km\, s}^{-1}$. This value is actually a lower limit because we are using a projected distance and an upper limit for the age of the relativistic electrons and, thus, it is consistent with the wind velocity ($V_{\mathrm{wind}} = 750\, \mathrm{km\, s}^{-1}$) inferred from the *N*-body/hydrodynamical simulations of RPS run for this particular case (see Merluzzi et al. 2016). The result of this simple calculation supports the scenario where the radio emission in the tail is fuelled by the relativistic electrons stripped from the galaxy.

The other parameter that informs us about the nature of the radio tail is the spectral index. Vollmer et al. (2009) found that the magnetic field and the warm ionised gas traced by Hα emission are closely linked in the Virgo galaxy NGC 4438 and that the spectral index of the extraplanar radio emission does not steepen with increasing distance from the galaxy disk implying an in situ re-acceleration of the relativistic electrons. This is different from what is observed in NGC 4522 (Vollmer et al. 2004) and NGC 4569 (Chyży et al. 2006), with the relativistic electrons showing a rapid aging with increasing distance. A steepening of the spectral index has been also reported by Chen et al. (2020) (see also Müller et al. 2021). The MeerKAT in-band spectral index shows that even the tail SOS 61086 steepens away from the location of the galaxy, reaching values up to $\alpha \sim -2$ at the end of the bright portion of the tail (see right panel of Fig. 9 and inset in the right panel of Fig. 8), consistent with synchrotron cooling, as expected for a radio emission due to relativistic electrons stripped from the galaxy.

We conclude that the radio tail revealed by MeerKAT observations in SOS 61086 is due to the ongoing RPS and is mainly related to relativistic electrons stripped from the galaxy disk.

SOS 61086 provides the observational evidence that RPS can also affect low mass galaxies in moderate- or low-density environments (Marcolini et al. 2003; Roediger & Hensler 2005). Moreover, it shows that ram pressure may act quite efficiently even when the galaxy orbit is not radial, with the stripped tail oriented almost tangentially to the cluster SC 1329–313.

This feature can be easily accommodated in the scenario suggested here: the minor merging between SC 1329–313 and A3562 would form the bridge of low surface brightness emission between the two clusters and further perturb the ICM (i.e. Owers et al. 2012), triggering RPS in SOS 61086.

Very recently, Roberts et al. (2021) identified 95 star forming galaxies experiencing ongoing RPS in low redshift ($z < 0.05$) clusters through 120−168 MHz radio continuum images from the LOFAR Two-meter Sky Survey. Hopefully, these data will shed light on the possible origin of the radio continuum emission in the tail of RPS galaxies.

6. Conclusions

In this paper, we present a radio study of the central region of the Shapley Supercluster, encompassing the two Abell clusters A3558 and A3562 and the two SC groups between them, SC 1327–312 and SC 1329–313. Our observations were carried out with ASKAP, MeerKAT, and GMRT, in a frequency range from 233 MHz to 1.656 GHz, and our analysis was complemented with *XMM-Newton* information and ESO-VST optical data.

Beyond the radio halo in A3562 and the radio source J1332–3146a, already imaged in previous works (V03, G05, V17), we have detected several new features. In particular:

- We revealed diffuse emission on the supercluster scale, covering the whole region between A3562 and SC 1329–313, corresponding to an extent of ∼1 Mpc. The emission has extremely low surface brightness, i.e. approximately 0.09 μJy arcsec^{-2}. It is the first time that diffuse emission between a cluster and a group is detected at GHz frequencies. It has the shape of a bridge connecting the radio halo in A3562 and SC 1329–313, plus a well-defined arc connecting the cluster and the SC group from the north. The equipartition magnetic field of this emission is very low, $H_{\rm eq} \sim 0.78$ μG, and the estimated age of the radiating electrons range between ∼86 Myr to ∼132 Myr depending on the assumptions on the spectral break. Such a timescale is much shorter than the scale of the merger, which is estimated to be 1 Gyr;
- The diffuse radio source J1332–3146a shows no hints of connection with the embedded compact radio emission associated with a bright galaxy in SC 1329–313. Its spectral properties are consistent with a re-acceleration origin;
- We identified a radio continuum tail induced by ram pressure affecting the galaxy SOS 61086 in SC 1329–313. This case shows that ram pressure stripping can involve both warm gas and radio-emitting plasma and highlights the role of cluster-cluster interaction in triggering it;
- A head-tail radio galaxy has been identified, whose tail is broken and culminates in a misaligned bar, as is now being observed in a number of clusters. The broken tail and the bar have a very steep spectrum. A preliminary analysis shows that the bar has very high fractional polarisation, which deserves further investigation;
- We detected diffuse radio emission at the centre of A3558 for the first time. The radio source is small in size compared to typical giant radio halos, at 400 × 200 kpc, it has an ultra steep spectrum, $\alpha^{1283\,\rm MHz}_{887\,\rm MHz} = -2.3 \pm 0.4$, and very low radio power, $P_{1283\,\rm MHz} = 6.85 \times 10^{22}$ W Hz^{-1}.

A comparison of our radio images with the X-ray emission and temperature map from *XMM-Newton* shows a tight correspondence between the arc and bridge of radio emission and similar features in the X-rays.

The radio arc and the bridge support the scenario of Finoguenov et al. (2004), who suggested an off-axis interaction between A3562 and SC 1329–313, the latter passing north of A3562 to reach its current location. The overall morphology of the radio halo in A3562, J1332–3146a and the radio tail of SOS 60861 are consistent with a perturbation coming from the north. We propose that the arc and the bridge could trace the channel of turbulence injected in the ICM by passage of SC 1329–313. The value we derived for the equipartition magnetic field is consistent with the estimates provided in G05 to support the turbulence needed to produce such emission.

The classification of the diffuse radio emission in A3558 is unclear, and this possibly reflects the fact that the cluster shows features of both cool-core and non-cool-core systems. Its overall radio properties, namely, its ultrasteep spectrum, small size, and extremely low radio power, are consistent with re-acceleration induced by sloshing. In addition, these details would lend support to the interpretation of the X-ray properties of the cluster as being due to sloshing induced by a perturber – most likely SC 1327–312 (Rossetti et al. 2007).

The location of the head-tail and bar in the ridge of X-ray emission just between SC 1327–312 and SC 1329–313, a region of enhanced temperature, coupled with the steep spectrum and high fractional polarisation in the bar, suggest interaction between these two low-mass SC groups. Unfortunately, the available X-ray observations are not deep enough to detect discontinuities in the ICM.

Our study shows that even minor mergers may leave detectable non-thermal signatures, such as Mpc-scale radio emission in the region between clusters and groups, as well as other extended features associated with early- and late-type cluster galaxies, which bear invaluable information on the formation of large-scale structures. Deeper X-ray and polarisation observations have been planned to further advance our understanding of the merger and accretion processes in the core of the Shapley Supercluster.

Acknowledgements. We thank the anonymous referee for helping the clarity of the paper. The Australian SKA Pathfinder is part of the Australia Telescope National Facility which is managed by CSIRO. Operation of ASKAP is funded by the Australian Government with support from the National Collaborative Research Infrastructure Strategy. ASKAP uses the resources of the Pawsey Supercomputing Centre. Establishment of ASKAP, the Murchison Radio-astronomy Observatory and the Pawsey Supercomputing Centre are initiatives of the Australian Government, with support from the Government of Western Australia and the Science and Industry Endowment Fund. We acknowledge the Wajarri Yamatji people as the traditional owners of the Observatory site. The MeerKAT telescope is operated by the South African Radio Astronomy Observatory (SARAO), which is a facility of the National Research Foundation, an agency of the Department of Science and Innovation. The National Radio Astronomy Observatory is a facility of the National Science Foundation operated by Associated Universities, Inc. The optical imaging is collected at the VLT Survey Telescope using the Italian INAF Guaranteed Time Observations. We thank the staff of the GMRT who made these observations possible. The GMRT is run by the Nationale Centre for Radio Astrophysics of the Tata Institute of Fundamental Research. T. Venturi and G. Bernardi acknowledge the support from the Ministero degli Affari Esteri e della Cooperazione Internazionale, Direzione Generale per la Promozione del Sistema Paese, Progetto di Grande Rilevanza ZA18GR02. R. Kale acknowledges the support of the Department of Atomic Energy, Government of India under project no. 12-R&D-TFR-5.02-0700. S. P. Sikhosana acknowledges funding support from the South African Radio Astronomy Observatory (SARAO) and the National Research Foundation (NRF). O. Smirnov's research is supported by the South African Research Chairs Initiative of the Department of Science and Technology and National Research Foundation.

References

Abell, G. O., Corwin, H. G., Jr., & Olowin, R. P. 1989, ApJS, 70, 1
Asad, K. M. B., Girard, J. N., de Villers, M., et al. 2021, MNRAS, 502, 2970

Bardelli, S., Pisani, A., Ramella, M., et al. 1998a, MNRAS, 300, 589
Bardelli, S., Zucca, E., Zamorani, G., et al. 1998b, MNRAS, 296, 599
Bardelli, S., De Grandi, S., Ettori, S., et al. 2002, A&A, 382, 17
Bonafede, A., Brunetti, G., Vazza, F., et al. 2021, ApJ, 907, 32
Botteon, A., van Weeren, R. J., Brunetti, G., et al. 2020a, MNRAS, 499, L11
Botteon, A., Brunetti, G., van Weeren, R. J., et al. 2020b, ApJ, 897, 93
Bourdin, H., & Mazzotta, P. 2008, A&A, 479, 307
Bourdin, H., Mazzotta, P., Markevitch, M., et al. 2013, ApJ, 764, 82
Briggs, D. S. 1995, BAAS, 27, 112.02
Brüggen, M., Reiprich, Y. H., Bulbul, E., et al. 2021, A&A, 647, A3
Brunetti, G., & Jones, T. W. 2014, Int. J. Mod. Phys. D., 23, 1430007
Brunetti, G., Giacintucci, S., Cassano, R., et al. 2008, Nature, 455, 944
Buote, D. A. 2001, ApJ, 553, L15
Camilo, F., Sholz, P., Serylak, M., et al. 2018, ApJ, 856, 180
Cassano, R., Ettori, S., Giacintucci, S., et al. 2010, ApJ, 721, L82
Cassano, R., Brunetti, G., Norris, R. P., et al. 2012, A&A, 548, A100
Cassano, R., Ettori, S., Brunetti, G., et al. 2013, ApJ, 777, 141
Cassano, R., Brunetti, G., Giocoli, C., et al. 2016, A&A, 593, A81
Chen, H., Sun, M., Yagi, M., et al. 2020, MNRAS, 496, 4654
Chengalur, J. N. 2013, NCRA Technical Report NCRA/COM/001
Chyży, K. T., Soida, M., Bomans, D. J., et al. 2006, A&A, 447, 465
Clarke, A. O., Scaife, A. M. M., Shimwell, T., et al. 2019, A&A, 627, A176
Cohen, A. S., & Clarke, T. E. 2011, AJ, 141, 149
Condon, J. J., Cotton, W. D., White, S. V., et al. 2021, ApJ, 917, 18
Crowl, H. H., Kenney, J. D. P., van Gorkom, J. H., et al. 2005, AJ, 130, 65
Cuciti, V., Cassano, R., Brunetti, G., et al. 2021, A&A, 647, A50
Dallacasa, D., Brunetti, G., Giacintucci, S., et al. 2009, ApJ, 699, 1288
De Filippis, E., Schindler, S., & Erben, T. 2005, A&A, 444, 387
de Gasperin, F., van Weeren, R. J., Brüggen, M., et al. 2014, MNRAS, 444, 3130
Di Gennaro, G., Venturi, T., Dallacasa, D., et al. 2018, A&A, 620, A25
Dopita, M., Hart, J., McGregor, P., et al. 2007, Ap&SS, 301, 255
Dopita, M., Rhee, J., Farage, C., et al. 2010, Ap&SS, 327, 245
Duchesne, S. W., Johnston-Hollitt, M., & Wilber, A. G. 2021a, PASA, 38, 10
Duchesne, S. W., Johnston-Hollitt, M., & Bartalucci, I. 2021b, PASA, 38, 5
Ettori, S., Bardelli, S., De Grandi, S., et al. 2000, MNRAS, 318, 239
Finoguenov, A., Henriksen, M. J., Briel, U., et al. 2004, ApJ, 611, 811
Gavazzi, G., Contursi, A., Carrasco, L., et al. 1995, A&A, 304, 325
Ge, C., Liu, R.-Y., Sun, M., et al. 2020, MNRAS, 497, 4704
Gendron-Marsolais, M., Hlavacek-Larrondo, J., van Weerene, R. J., et al. 2020, MNRAS, 499, 5791
Ghizzardi, S., Rossetti, M., & Molendi, S. 2010, A&A, 516, A32
Giacintucci, S., Venturi, T., Bardelli, S., et al. 2004, A&A, 419, 71
Giacintucci, S., Venturi, T., Brunetti, G., et al. 2005, A&A, 440, 867
Giacintucci, S., Venturi, T., Markevitch, M., et al., 2022, ApJ, submitted
Govoni, F., Orrú, E., Bonafede, A., et al. 2019, Science, 364, 981
Haines, C. P., Merluzzi, P., Mercurio, A., et al. 2006, MNRAS, 371, 55
Haines, C. P., Busarello, G., Merluzzi, P., et al., 2011, MNRAS, 412, 145
Haines, C. P., Busarello, G., Merluzzi, P., et al. 2018, MNRAS, 481, 1055
Higuchi, Y., Okabe, N., Merluzzi, P., et al. 2020, MNRAS, 497, 52
Hotan, A. W., Bunton, J. D., Chippendale, A. P., et al. 2021, PASA, 38, 9
Hudson, H. S., Mittal, R., Reiprich, T. H., et al. 2010, A&A, 513, A37
Hugo, B. V., et al. 2022, XXX ADASS Conference, ASP Conf. Ser., in press
Intema, H. T., van der Tol, S., Cottonw, W. D., et al. 2009, A&A, 501, 1185
Jones, D. H., Read, M. A., Saunders, W., et al. 2009, MNRAS, 399, 683
Jonhnston, S., Taylor, R., Bailes, M., et al. 2008, Exp. Astron., 22, 151
Józsa, G. I. G., White, S. V., Thorat, K., et al. 2020, ASP Conf. Ser., 527, 635
Józsa, G. I. G., White, S. V., Thorat, K., et al. 2022, XXX ADASS Conference, ASP Conf. Ser., in press
Kalberla, P. M. W., Burton, W. B., & Hartmann, D. 2005, A&A, 440, 775
Kale, R., Venturi, T., Cassano, R., et al. 2015, A&A, 581, A23
Kenyon, J. S., Smirnov, O. M., Grobler, T. L., et al. 2018, MNRAS, 478, 2399
Killeen, N. E. B., & Bicknell, G. V. 1988, ApJ, 324, 198
Kim, K.-T., Kronberg, P. P., Giovannini, G., et al. 1989, Nature, 341, 720
Knowles, K., Cotton, W. D., Rudnick, L., et al. 2022, A&A, 657, A56
Kuntz, K. D., & Snowden, S. L. 2000, ApJ, 543, 195
Liang, H., Hunstead, R. W., Birkinshaw, M., et al. 2000, ApJ, 544, 686
Marcolini, A., Brighenti, F., & D'Ercole, A. 2003, MNRAS, 345, 1329
Markevitch, M., & Vikhlinin, A. 1997, ApJ, 474, 84
Mercurio, A., Merluzzi, P., Haines, C. P., et al. 2006, MNRAS, 368, 109
Mercurio, A., Merluzzi, P., Busarello, G., et al. 2015, MNRAS, 453, 3685
Merluzzi, P., Busarello, G., Dopita, M. A., et al. 2013, MNRAS, 429, 1747
Merluzzi, P., Busarello, G., Heines, C. P., et al. 2015, MNRAS, 446, 803
Merluzzi, P., Busarello, G., Dopita, M. A., et al. 2016, MNRAS, 460, 3345
Müller, A., Poggianti, B., Pfrommer, C., et al. 2021, Nat. Astron., 5, 159
Nolting, C., Jones, T. W., O'Neill, B. J., et al. 2019, ApJ, 876, 154
Noordam, J. E., & Smirnov, O. M. 2010, A&A, 524, A61
Norris, R. P., Hopkins, A. M., Afonso, J., et al. 2011, PASA, 28, 215
Owers, M. S., Couch, W. J., Nulsen, P. E. J., et al. 2012, ApJ, 750, L23
Offringa, A. R., & Smirnov, O. 2017, MNRAS, 471, 301
Offringa, A. R., McKinley, B., Hurley-Walker, N., et al. 2014, MNRAS, 444, 606
Perley, R. A., & Butler, B. J. 2013, ApJS, 204, 19
Quintana, H., Ramirez, A., Melnick, J., et al. 1995, AJ, 110, 463
Quintana, H., Melnick, J., Proust, D., et al. 1997, A&AS, 125, 247
Planck Collaboration XXIX. 2013, A&A, 571, A29
Ragagnin, A., Saro, A., Priyanca, S., et al. 2021, MNRAS, 500, 5056
Raychaudhury, S. 1989, Nature, 342, 251
Reynolds, J. E. 1994, A Revised Flux Scale for the AT Compact Array, Technical Report 39.3/040 (Australia Telescope National Facility)
Roberts, I. D., van Weeren, R. J., McGee, S. L., et al. 2021, A&A, 650, A111
Roediger, E., & Hensler, G. 2005, A&A, 2005, 433
Rossetti, M., Ghizzardi, S., Molendi, S., et al. 2007, A&A, 463, 839
Rossetti, M., Eckert, D., De Grandi, S., et al. 2013, A&A, 556, A44
Rudnick, L. 2002, PASP, 114, 427
Savini, F., Bonafede, A., Brüggen, M., et al. 2019, A&A, 622, A24
Scaife, A. M. M., & Heald, G. H. 2012, MNRAS, 423, L30
Scaramella, R., Baiesi-Pillastrini, G., Chincarini, G., et al. 1989, Nature, 338, 562
Schuecker, P., Böhringer, H., Reiprich, T. H., et al. 2001, A&A, 378, 408
Shapley, H. 1930, Harv. Coll. Obs. Bull., 874, 9
Shimwell, T. W., Luckin, J., Brüggen, M., et al. 2016, MNRAS, 459, 277
Skinner, C. J., Becker, R. H., White, R. L., et al. 1998, MNRAS, 296, 669
Smith, R. K., Brickhouse, N. S., Liedahl, D. A., et al. 2001, ApJ, 556, L91
Starck, J.-L., Fadili, J. M., Digel, S., et al. 2009, A&A, 504, 641
Stassun, K. G., Oelkers, R. J., Paegert, M., et al. 2019, AJ, 158, 138
van Haarlem, M. P., Wise, M. W., Gunst, A. W., et al. 2013, A&A, 556, A2
van Weeren, R. J., de Gasperin, F., Akamatsu, H., et al. 2019, Space Sci. Rev., 215, 16
van Weeren, R. J., Shimwell, T. W., Botteon, A., et al. 2021, A&A, 651, A115
Venturi, T., Bardelli, S., Morganti, R., et al. 1996, MNRAS, 285, 898
Venturi, T., Bardelli, S., Morganti, R., et al. 2000, MNRAS, 314, 594
Venturi, T., Bardelli, S., Dallacasa, D., et al. 2003, A&A, 402, 913
Venturi, T., Giacintucci, S., Brunetti, G., et al. 2007, A&A, 463, 937
Venturi, T., Bardelli, S., Dallacasa, D., et al. 2017a, Galaxies, 5, 16
Venturi, T., Rossetti, M., Brunetti, G., et al. 2017b, A&A, 603, A125
Vettolani, G., Chincarini, G., Scaramella, R., et al. 1990, AJ, 99, 1709
Vollmer, B., Beck, R., Kenney, J. D. P., et al. 2004, AJ, 127, 3375
Vollmer, B., Soida, M., Chung, A., et al. 2009, A&A, 496, 669
Zhang, B., Fadili, M., & Starck, J.-L. 2008, IEEE Trans. Image Process., 17, 1093
Zhang, C., Churazov, E., Forman, W. R., et al. 2019, MNRAS, 488, 5259
Zucca, E., Zamorani, G., Scaramella, R., et al. 1993, ApJ, 407, 470

[1] INAF – Istituto di Radioastronomia, Via Gobetti 101, 40129 Bologna, Italy
e-mail: tventuri@ira.inaf.it
[2] Naval Research Laboratory, 4555 Overlook Avenue SW, Code 7213, Washington, DC 20375, USA
[3] INAF – Osservatorio Astronomico di Capodimonte, Via Moiariello 16, 80131 Napoli, Italy
[4] INAF – Osservatorio di Astrofisica e Scienza dello Spazio di Bologna, Via Gobetti 93/3, 40129 Bologna, Italy
[5] Dipartimento di Fisica e Astronomia, Universita di Bologna, Via Gobetti 93/2, 40129 Bologna, Italy
[6] Astrophysics Research Centre, University of KwaZulu-Natal, Durban 4041, South Africa
[7] School of Mathematics, Statistics, and Computer Science, University of KwaZulu-Natal, Westville 3696, South Africa
[8] NRAO, PO Box 0, Soccoro, NM 87801, USA
[9] Department of Physics and Electronics, Rhodes University, PO Box 94, Makhanda 6140, South Africa
[10] South African Radio Astronomy Observatory, 2 Fir Street, Black River Park, Observatory, Cape Town 7925, South Africa
[11] Universitá di Roma Tor Vergata, Via della Ricerca Scientifica, 00133 Roma, Italy
[12] IASF-Milano, INAF, Via A. Corti 12, 20133 Milano, Italy
[13] Minnesota Institute for Astrophysics, University of Minnesota, 116 Church St. SE, Minneapolis, MN 55455, USA
[14] Hamburger Sternwarte, Universität Hamburg, Gojenbergsweg 112, 21029 Hamburg, Germany

[15] Leiden Observatory, Leiden University, PO Box 9513, 2300 RA Leiden, The Netherlands
[16] National Centre for Radio Astrophysics, Tata Institute of Fundamental Research, S. P. Pune University Campus, Ganeshkhind, Pune 411007, India
[17] Australia Telescope National Facility, CSIRO Astronomy and Space Science, PO Box 76, Epping, NSW 1710, Australia
[18] Western Sydney University, Locked Bag 1797, Penrith, NSW 2751, Australia
[19] Astrophysics, Department of Physics, University of Oxford, Keble Road, Oxford OX1 3RH, UK
[20] Department of Physics and Electronics, Rhodes University, PO Box 94, Makhanda 6140, South Africa
[21] Australian Astronomical Optics, Macquarie University, 105 Delhi Rd, North Ryde, NSW 2113, Australia
[22] Argelander-Institut für Astronomie, Universität Bonn, Auf dem Hügel 71, 53121 Bonn, Germany
[23] GEPI & USN, Observatoire de Paris, CNRS, Universite Paris Diderot, 5 place Jules Janssen, 92190 Meudon, France
[24] Centre for Radio Astronomy Techniques and Technologies, Department of Physics and Electronics, Rhodes University, Grahamstown 6140, South Africa
[25] CSIRO Astronomy and Space Science, PO Box 1130, Bentley, WA 6102, Australia
[26] Instituto de Fisica de Cantabria, CSIC-Universidad de Cantabria, 39005 Santander, Spain

Appendix A: GMRT images

In this appendix, we show the primary beam corrected images of the GMRT observations presented in Table 2. The location of the various features studied in this paper are highlighted in each image. Since we did not use the observations at 608 MHz of project 22_039 in this paper, we do not show those images.

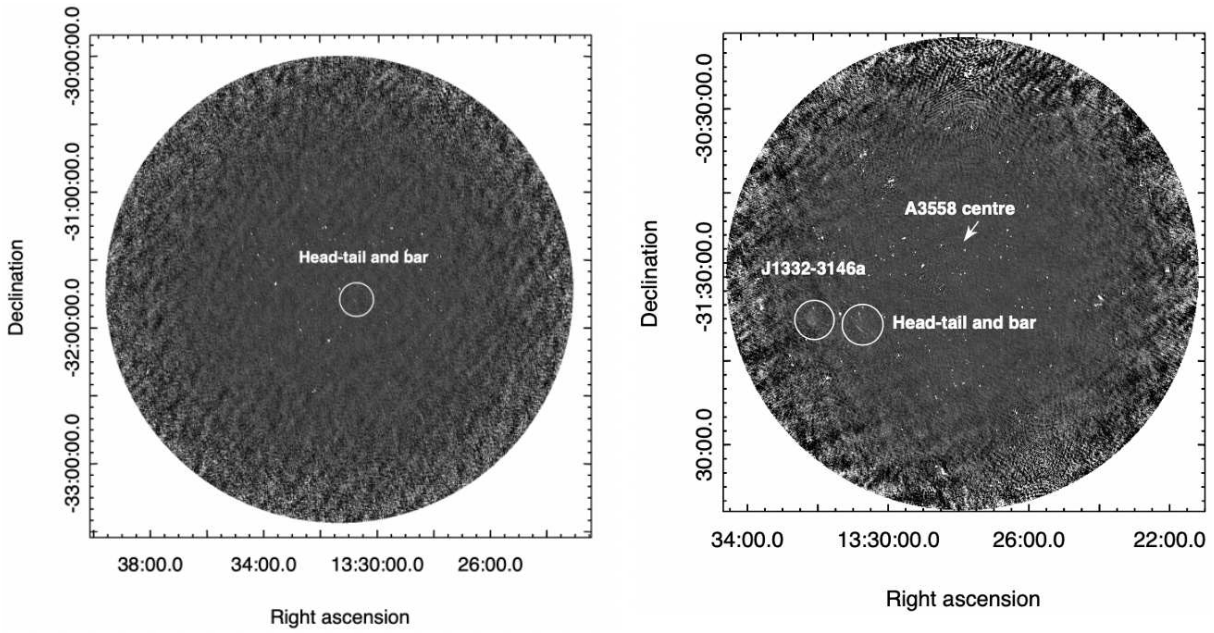

Fig. A.1. Primary beam corrected 233 MHz GMRT image of the project 30_024 (see Table 2 and Fig. 2), shown in the left panel. The angular resolution is 24.4″ × 10.7″, p.a. 26°. The location of the head-tail and the bar has been highlighted. The right panel shows the primary beam corrected 306 MHz GMRT image of the project 22_039 (see Table 2 and Fig. 2). The angular resolution is 14.0″ × 9.5″, p.a. 18.4°. The location of J 1332–3146a, head-tail, bar, and A 3558 centre have been highlighted.

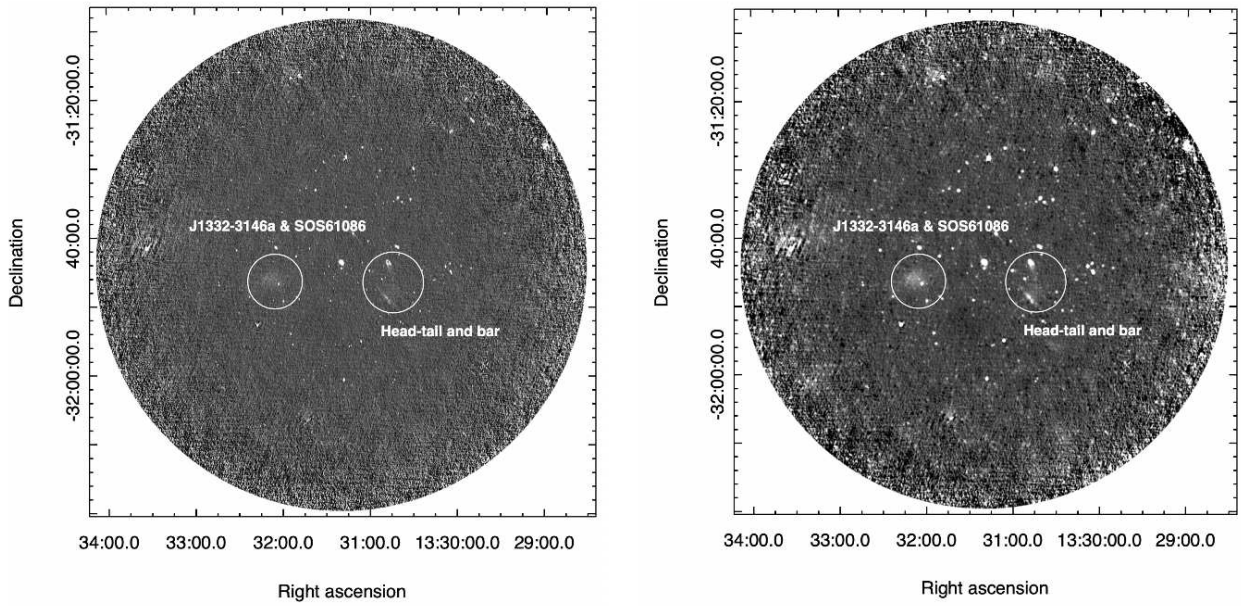

Fig. A.2. Primary beam corrected 607 MHz GMRT images of the project 30_024 (see Table 2, Fig. 2, and Sect. 4.5). Location of J 1332–3146a, SOS 61086, head-tail, and bar have been highlighted. Left panel: Angular resolution is 9.7″ × 5.5″, p.a. 9.6°. Right panel: Angular resolution: 15″ × 15″.